

# Targeted protein relocalization via protein transport coupling

<https://doi.org/10.1038/s41586-024-07950-8>

Christine S. C. Ng<sup>1</sup>, Aofei Liu<sup>1</sup>, Bianxiao Cui<sup>1</sup> & Steven M. Banik<sup>1,2</sup>✉

Received: 14 September 2023

Accepted: 14 August 2024

Published online: 18 September 2024

 Check for updates

Subcellular protein localization regulates protein function and can be corrupted in cancers<sup>1</sup> and neurodegenerative diseases<sup>2,3</sup>. The rewiring of localization to address disease-driving phenotypes would be an attractive targeted therapeutic approach. Molecules that harness the trafficking of a shuttle protein to control the subcellular localization of a target protein could enforce targeted protein relocalization and rewire the interactome. Here we identify a collection of shuttle proteins with potent ligands amenable to incorporation into targeted relocalization-activating molecules (TRAMs), and use these to relocalize endogenous proteins. Using a custom imaging analysis pipeline, we show that protein steady-state localization can be modulated through molecular coupling to shuttle proteins containing sufficiently strong localization sequences and expressed in the necessary abundance. We analyse the TRAM-induced relocalization of different proteins and then use nuclear hormone receptors as shuttles to redistribute disease-driving mutant proteins such as SMARCB1<sup>Q318X</sup>, TDP43<sup>ΔNLS</sup> and FUS<sup>R495X</sup>. TRAM-mediated relocalization of FUS<sup>R495X</sup> to the nucleus from the cytoplasm correlated with a reduction in the number of stress granules in a model of cellular stress. With methionyl aminopeptidase 2 and poly(ADP-ribose) polymerase 1 as endogenous cytoplasmic and nuclear shuttles, respectively, we demonstrate relocalization of endogenous PRMT9, SOS1 and FKBP12. Small-molecule-mediated redistribution of nicotinamide nucleotide adenylyltransferase 1 from nuclei to axons in primary neurons was able to slow axonal degeneration and pharmacologically mimic the genetic WldS gain-of-function phenotype in mice resistant to certain types of neurodegeneration<sup>4</sup>. The concept of targeted protein relocalization could therefore inspire approaches for treating disease through interactome rewiring.

Spatiotemporal control of subcellular protein localization creates a coordinated system to regulate cellular physiology<sup>5</sup>. Aberrant trafficking and localization of proteins underlies numerous diseases, including cancers<sup>6,7</sup>, neurodegenerative diseases<sup>3,8</sup> and genetic disorders<sup>9</sup>. Mutations that reroute tumour suppressor proteins from the nucleus to the cytoplasm are common mechanisms for promoting oncogenesis. Translocation of RNA-binding proteins such as TDP43 and fused in sarcoma (FUS) to the cytoplasm is a hallmark of amyotrophic lateral sclerosis (ALS)<sup>2</sup> and has numerous deleterious phenotypic consequences, including increased cytoplasmic aggregates<sup>10–12</sup>. Correcting these phenotypes through selective inhibition of a protein's trafficking presents several challenges, given the conserved nature of nuclear export and import machinery. The global toxicity of nuclear import or export inhibition has restricted the application of molecules that target these pathways<sup>13,14</sup>. Yet, the limited clinical success of global nuclear export inhibitors such as selinexor in certain contexts<sup>15,16</sup> suggests that targeted approaches to the control of protein trafficking could potentiate alternative therapeutic strategies.

The ability to exert targeted, pharmacological control of the subcellular location of an individual protein could provide avenues for

addressing intractable diseases, as function-blocking molecules address only a small number of disease-relevant activities<sup>17</sup>. Gain-of-function molecules that directly drive the formation of neocomplexes between proteins lift several constraints that restrict the range of viable therapeutic targets<sup>18,19</sup>. In the context of controlling subcellular localization, correcting diseased phenotypes that result directly from protein mislocalization or imparting beneficial function through protein relocation could expand the range of therapeutic options. A selection of tools for studying protein sequestration upon different stimuli with synthetic protein fusions to nuclear hormone receptor ligand-binding domains<sup>20,21</sup>, LOV2 domains<sup>22,23</sup> or binding sites for localization sequence-containing nanobodies<sup>24</sup> have enabled fundamental studies of altered protein localization. Early work that used chemically induced proximity between FRB and FKBP12 fused to arrayed localization sequences driven by rapamycin demonstrated the potential of small-molecule control over localization programming<sup>25–27</sup>. This approach was extended to the rapid sequestration of cytoplasmic and endosomal proteins onto mitochondrial surfaces to attenuate activity<sup>28</sup>. Chemical control over localization has also been demonstrated with molecules that consist of protein-binding warheads linked to DNA intercalators<sup>29</sup> and membrane-targeting lipids<sup>30</sup>.

<sup>1</sup>Department of Chemistry, Stanford University, Stanford, CA, USA. <sup>2</sup>Sarafan ChEM-H, Stanford University, Stanford, CA, USA. ✉e-mail: sbanik@stanford.edu

Therapeutic modulation of target protein location by means of coupling to a cellular shuttle or anchor protein provides an alternative avenue for programmable molecular control. To advance the idea of localization control to address disease-driving proteins, an understanding of the cellular features that enable localization hijacking and expansion of the viable targets, molecules and mechanistic principles of transport control is needed. A quantitative analysis of localization reprogramming ability would greatly facilitate the extension of small-molecule-mediated protein relocation to therapeutic contexts. Here we develop a quantitative approach to demonstrate targeted protein relocation by means of targeted relocation-activating molecules (TRAMs), which couple the trafficking of a target protein to the trafficking of a shuttle protein (Fig. 1a). We demonstrate the ability to use nuclear hormone receptors to mediate nuclear import of disease-relevant mutant proteins, and methionyl aminopeptidase 2 (METAP2) and poly(ADP-ribose) polymerase 1 (PARP1) as endogenous shuttles to redistribute endogenous proteins. Finally, we use targeted relocation by means of a TRAM to generate a gain-of-function protective phenotype in a model of neurodegeneration. Through coupling shuttles and targets using drug-like molecules, we advance approaches for therapeutic modulation of cellular physiology on the basis of the concept of controlled protein trafficking.

## Demonstration of TRAM-induced relocation

Nuclear localization sequences (NLSs) and nuclear export sequences (NESs) are recognized by members of the karyopherin family of proteins to regulate bidirectional transport of cargo between the nucleus and the cytoplasm<sup>31</sup>. We reasoned that overcoming the inherent localization of a protein by means of protein transport coupling would require (1) a sufficiently strong opposing localization sequence on the shuttling protein and (2) a requisite stoichiometry of shuttle protein. To examine these parameters, we chose nicotinamide nucleotide adenyllyltransferase 1 (NMNAT1) as a model nuclear-localized target protein for relocation. We hypothesized that as NMNAT1 possesses only a single predicted NLS and no known direct DNA-binding domain, it might be susceptible to small-molecule-mediated relocation. To enable the study of proteins lacking known small-molecule binders, we synthesized the bifunctional molecule **1** (Fig. 1b), which engages the *Escherichia coli* dihydrofolate reductase domain (*EcDHFR*) and the FKBP12<sup>F36V</sup> domain, both of which have found widespread use owing to their tight binding affinities and orthogonality to most mammalian proteins. We generated an mCherry fusion to *EcDHFR* and the NES from the HIV-1 REV protein<sup>32</sup> to act as a shuttle protein. As transient transfection results in a range of confounding variables for examining the relative stoichiometries between two proteins and results in high levels of transgene expression<sup>33</sup>, we stably incorporated mCherry–*EcDHFR*-NES and FKBP12<sup>F36V</sup>-GFP-NMNAT1 into HeLa cells (Fig. 1c). Complex formation between both partners mediated by **1** was demonstrated by co-immunoprecipitation (Fig. 1d). We isolated clonal export line A (EL-A) with a relative mCherry/GFP median fluorescence intensity ratio of 1.0, which demonstrated dose-dependent translocation of NMNAT1 to the cytoplasm upon treatment with **1** (Fig. 1e), an effect that was abrogated at higher concentrations. Simultaneous treatment with the unlinked warheads **2** and **3** had no effect on protein localization (Extended Data Fig. 1a,b). Compound **1a**, containing a longer linker between the two warheads, afforded a similar relocation ability to **1** (Extended Data Fig. 1a,j,k). The quantification of nucleocytoplasmic transport when studying two proteins simultaneously has traditionally been done by a colocalization metric across a set of representative images. We reasoned that an open-source computational imaging analysis pipeline that provides single-cell-level analysis of two different proteins independently in both the nucleus and cytoplasm would be the most accurate approach for gauging protein transport and comparing different target proteins

and shuttle proteins (Fig. 1f). We built this custom analysis pipeline by first segmenting cells using a nuclear stain reference, then masking cells to capture both a nuclear area and cytoplasmic area. We applied a gating filter on nuclear intensities to remove aberrantly high nuclear-stained objects such as debris and dead cells. Finally, we summed and averaged the intensities per cell for the nuclear masked area and cytoplasmic masked area to give a pixel intensity per area measurement akin to the relative concentration of fluorophore in the nucleus and cytoplasm for each cell. We verified that this approach would be applicable to different cell types and densities (Extended Data Fig. 2a–d).

Quantitative analysis was used to examine dose-, shuttle protein- and stoichiometry-dependent relocation. We observed a concentration-dependent hook effect with **1** on the transport of NMNAT1 (Fig. 1g). Quantification of relocation also revealed that although NMNAT1 was readily extracted to the cytoplasm with **1**, NMNAT1 did not possess a sufficiently strong NLS to partially redistribute mCherry–*EcDHFR*-NES to the nucleus. To examine the impact of relative stoichiometry between NMNAT1 and *EcDHFR*-NES, we isolated two more clonal export cell lines (EL-B and EL-C) with varying mCherry/GFP ratios (Extended Data Fig. 1c). When treated with **1**, cell lines with higher mCherry/GFP ratios exhibited a high degree of NMNAT1 redistribution to the cytoplasm (Fig. 1h). Cell lines with intermediate ratios resulted in diffuse NMNAT1 localization. EL-C, with the lowest relative expression levels of mCherry to GFP, exhibited 10% NMNAT1 relocation upon treatment with **1** (Extended Data Fig. 1d). When cells were co-treated with leptomycin-B, an inhibitor of nuclear export by exportin 1, along with **1**, no relocation of NMNAT1 was observed and an enrichment in nuclear mCherry resulted (Extended Data Fig. 1d–g). Similar to EL-A, co-treatment with **2** and **3** did not cause protein relocation in EL-B or EL-C (Extended Data Fig. 1d–g). No degradation was observed as a function of **1** in four clonal cell lines (Extended Data Fig. 1h,i). These results support active NES-driven redistribution of NMNAT1 through small-molecule-mediated coupling.

To examine whether diffuse proteins can be sequestered in the nucleus by non-DNA-binding proteins, we generated cell lines stably expressing mCherry–*EcDHFR* without an NES and FKBP12<sup>F36V</sup>-GFP–NMNAT1. We isolated clonal import cell lines A–C (IL-A–C) with relative mCherry/GFP ratios spanning three orders of magnitude (Extended Data Fig. 3c) and analysed their ability to sequester mCherry upon treatment with **1**. The initial percentage of nuclear mCherry was approximately 50% in all cell lines, consistent with diffuse localization. After treatment with **1**, lines IL-A and IL-B with relative mCherry/GFP ratios of 0.001 and 0.01, respectively, were both capable of significant sequestration of mCherry (80% nuclear) (Fig. 1i,j and Extended Data Fig. 3a,d,e). Co-treatment with **2** and **3** had no effect on mCherry localization (Extended Data Fig. 3b). IL-C, with a relative mCherry/GFP ratio of 1.0, did not exhibit a large enrichment of nuclear mCherry upon treatment with **1** (Extended Data Fig. 3d,f). No diffusion of FKBP12<sup>F36V</sup>-GFP–NMNAT1 was observed in cells due to coupling to mCherry–*EcDHFR* (Extended Data Fig. 3g). Treatment with **1** did not lead to degradation of either mCherry or NMNAT1 in all four clonal cell lines (Extended Data Fig. 3h,i). Together, these data demonstrate that sufficient levels of anchor or shuttle must be present to enforce TRAM-induced relocation of a target protein.

In principle, the trafficking of any protein could relocate another provided suitable localization strength, expression levels and effective molecular coupling. Nuclear hormone receptors such as the oestrogen receptor (ER $\alpha$ ) and glucocorticoid receptor (GR) exhibit ligand-dependent translocation from the cytoplasm to the nucleus to exert downstream transcriptional activation. Several agonists or antagonists of nuclear hormone receptors could be repurposed to hijack the nuclear trafficking capabilities of these proteins (Extended Data Fig. 4d). These ligands have previously been incorporated into bifunctional molecules that act as degraders or transcriptional

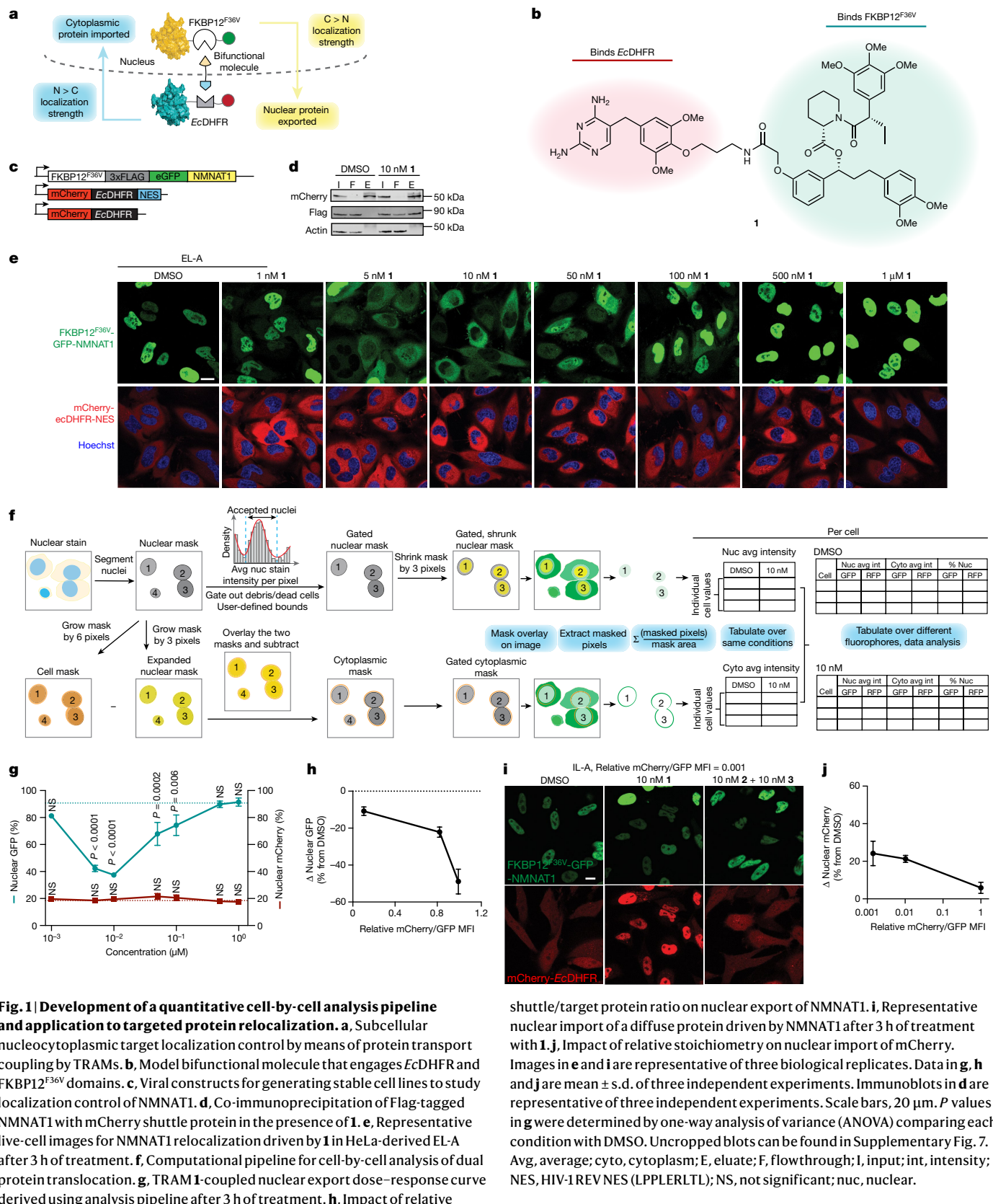


**Fig. 1 | Development of a quantitative cell-by-cell analysis pipeline and application to targeted protein relocalization.** **a**, Subcellular nucleocytoplasmic target localization control by means of protein transport coupling by TRAMs. **b**, Model bifunctional molecule that engages EcDHFR and FKBP12<sup>F36V</sup> domains. **c**, Viral constructs for generating stable cell lines to study localization control of NMNAT1. **d**, Co-immunoprecipitation of Flag-tagged NMNAT1 with mCherry shuttle protein in the presence of **1**. **e**, Representative live-cell images for NMNAT1 relocalization driven by **1** in HeLa-derived EL-A after 3 h of treatment. **f**, Computational pipeline for cell-by-cell analysis of dual protein translocation. **g**, TRAM1-coupled nuclear export dose-response curve derived using analysis pipeline after 3 h of treatment. **h**, Impact of relative

shuttle/target protein ratio on nuclear export of NMNAT1. **i**, Representative nuclear import of a diffuse protein driven by NMNAT1 after 3 h of treatment with **1**. **j**, Impact of relative stoichiometry on nuclear import of mCherry. Images in **e** and **i** are representative of three biological replicates. Data in **g**, **h** and **j** are mean  $\pm$  s.d. of three independent experiments. Immunoblots in **d** are representative of three independent experiments. Scale bars, 20  $\mu$ m. *P* values in **g** were determined by one-way analysis of variance (ANOVA) comparing each condition with DMSO. Uncropped blots can be found in Supplementary Fig. 7. Avg, average; cyto, cytoplasm; E, elutet; F, flowthrough; I, input; int, intensity; NES, HIV-1 REV NES (LPPLERLTL); NS, not significant; nuc, nuclear.

activators<sup>34–37</sup>. To demonstrate the potential of these receptors as nuclear shuttles, we synthesized **4–7** (Extended Data Figs. 4a, 5a, 6a and 7a), which use dexamethasone- and raloxifene-based warheads known to engage but not downregulate GR and ER $\alpha$ . Using ectopically

expressed model constructs, we validated that these molecules engage GR and ER $\alpha$  to nuclear enhance FKBP12 and FKBP12<sup>F36V</sup>, and that ternary complex formation is necessary for this relocalization (Extended Data Figs. 4–7).

## Shuttle–target pairs determine relocalizability

To effectively relocalize a target protein, a TRAM must sufficiently engage a shuttle protein capable of overcoming the target's intrinsic localization. Quantification of the relative relocalization ability of proteins could enable rational choices of shuttle–target combinations. To develop a metric that details a protein's relative relocalization ability, we generated polyclonal cell lines containing a set of genetic constructs pairing GR and ER $\alpha$  against well-characterized NESs (Fig. 2a). We treated our GR or ER $\alpha$  lines containing NES-tagged targets with varying concentrations of the relevant TRAM (**4** or **5**), then assessed the relocalization of the NES-tagged protein as well as the nuclear hormone receptor (Fig. 2b,c and Supplementary Figs. 1 and 2). We observed variable degrees of target relocalization that depended on both the shuttle identity (ER $\alpha$  or GR) and the NES sequence of the target. For GR, we observed ligand-activated relocalization. ER $\alpha$  remained nuclear regardless of the presence of TRAM. Despite different relative steady-state distributions of ER $\alpha$  and GR before TRAM treatment, the relative relocalizabilities of the NES-tagged target proteins remained consistent. ER $\alpha$  was able to partially relocalize the HIV-1 REV NES-containing protein, whereas the HIV-1 REV NES-containing protein caused partial nuclear export of GR (Fig. 2c). To analyse the relative strength of a small panel of NLSs, we paired them against HIV-1 REV NES (Fig. 2d) using **1** and observed a gradation in the relocalization ability of the different NLS constructs. Combined, these data highlight the importance of shuttle protein choice in effecting the desired degree of target protein relocalization.

We previously observed a correlation of shuttle-to-target ratio with the degree of TRAM-induced relocalization. Using a doxycycline-inducible promoter system, we generated a heterogeneous population of cells containing each pair of proteins which enabled a comparison of the effects of shuttle-to-target ratios across sequences and receptors. We used our image analysis pipeline to estimate the ratios between fluorophores on a single-cell basis. This analysis was validated by comparison with ratios obtained from manual integration of fluorophore intensity in TRAM-induced nuclear import and export experiments. We then applied this analysis to the comparative NES and NLS relocalization datasets (Supplementary Fig. 3). For each pair, we derived best-fit dose-response curves from data examining protein localization as a function of the relative shuttle-to-target ratio on a per cell basis throughout the entire population (Supplementary Fig. 4). From this analysis we calculated the theoretical maximum relocalization of a target as well as the sensitivity of that target's relocalization to the relative ratio of shuttle-to-target protein. To compare optimal dose-response curves, we selected the concentrations of TRAM that resulted in the highest theoretical maximum movement for each target. We then compared each of the four NES sequences paired with ER $\alpha$  or GR and observed that the effective ratio (ER $_{50}$ ) for relocalization was lower for each NES when paired with ER $\alpha$  and the theoretical maximum degree of relocalization was higher (Fig. 2e). Although we were not able to distinguish the relative relocalizability between HIV-1 REV NES and MEK1 NES using ER $\alpha$  as a shuttle, we saw clear differences when employing GR as a shuttle protein (Fig. 2f). Thus, we were able to distinguish relative relocalizability between targets by comparing them among different shuttles. Cells with lower ratios of GR to HIV-1 REV NES abolished TRAM-mediated nuclear GR enhancement, and resulted in GR nuclear export (Fig. 2g). Similarly, we compared the ability of different NLS sequences to be relocalized by the HIV-1 REV NES. We observed a clear trend in relocalization across different NLSs, demonstrating this analysis can be applied to both nuclear import and export (Fig. 2h). Together, these data enable quantitative comparisons of relocalization across target proteins and shuttle proteins as a function of protein ratios. We developed a metric in which numerical difference from zero reflects the degree of relocalizability. We normalized the observed change in target localization by

the absolute difference between the steady-state localization and complete sequestration in that compartment (Fig. 2i). The relative ranking for relocalization scores among the four NES sequences examined was IKBa > P53 > MEK1 > HIV-1 REV. Likewise, the relative ranking for relocalizability of the NLS sequences was NMNAT1 > SV40 > P53 > NPM1. By combining relocalizability with a steady-state distribution descriptor, we generated a localization score that allows us to differentiate the localization strengths of proteins with similar steady-state distributions, such as HIV-1 REV and MEK1 (Fig. 2j). Across the NLS series, we observed that localization strength paralleled relocalizability (Fig. 2k,l). These metrics suggest intrinsic relocalization abilities for certain sequences and shuttles and imply a hierarchy that may be inferred from differential pairings of candidate shuttles and targets.

## Mislocalized mutant protein relocalization

Mislocalized transcriptional regulators and RNA-binding proteins are hallmarks of several cancers and neurodegenerative diseases. Targeted approaches that return these proteins to the nucleus might help to ameliorate disease-driving phenotypes. We examined the ability to relocalize three mutant proteins known to exhibit aberrant localization in disease. SMARCB1<sup>Q318X</sup> is a mutant C-terminal truncation of SMARCB1 found in atypical teratoid and rhabdoid tumours that has been reported to exhibit cytoplasmic localization<sup>38</sup>. Mislocalized TDP43 mutants lacking NLS sequences (TDP43<sup>ΔNLS</sup>) that seed aggregates in the cytoplasm are a conserved biomarker for ALS<sup>39</sup>. Mutations in the FUS protein that alter its nuclear localization have been observed in patients with ALS<sup>40</sup>. The FUS<sup>R495X</sup> mutation is associated with an aggressive disease phenotype<sup>41</sup>, and forms cytoplasmic granules in neurons that have been linked to its pathogenic function<sup>42</sup>.

We engineered HeLa cells to constitutively express each mutant along with ER $\alpha$  on a doxycycline-inducible promoter (Fig. 3a). Upon addition of doxycycline and subsequent treatment with **5**, we observed that the requisite relative ratio of ER $\alpha$  to each mutant required for maximum relocalization was achieved in different fractions of each population (Fig. 3b,c and Extended Data Fig. 8a–d). Mean population analysis showed significant relocalization across all concentrations of TRAM for each mutant (Extended Data Fig. 8e) and no ligand-induced protein stabilization (Extended Data Fig. 8f). Best-fit curves allowed us to extract the theoretical maximum relocalization of each mutant (Fig. 3d and Supplementary Fig. 5), from which we derived the relative relocalizability and localization strength of each mutant when paired with ER $\alpha$  (Fig. 3e). We observed that TDP43<sup>ΔNLS</sup> and FUS<sup>R495X</sup> were more readily relocalized by ER $\alpha$  than SMARCB1<sup>Q318X</sup>, suggesting protein-intrinsic features that facilitate or hinder relocalization.

We hypothesized that FUS<sup>R495X</sup>-positive cytoplasmic granules might be dissolved if TRAMs could induce redistribution of FUS<sup>R495X</sup> to the nucleus. To assess protein extraction from granules, we examined FUS<sup>R495X</sup>-expressing HeLa cells treated with sodium arsenite to instigate stress granule formation (Fig. 3f). After formation of granules, cells were treated with **5** and continuously imaged (Fig. 3g). We observed relocalization of FUS<sup>R495X</sup> from both granules and the cytoplasm to the nucleus over the course of 2 h after exposure to **5** (Fig. 3h and Extended Data Fig. 9a,b). These observations are consistent with small-molecule-mediated extraction of FUS<sup>R495X</sup> from cytoplasmic granules to the nucleus. To quantify the effect of FUS<sup>R495X</sup> redistribution on the number of stress granules in cells, we performed fixed-cell immunofluorescence imaging to examine both mCherry–FKBP12<sup>F36V</sup>–FUS<sup>R495X</sup> and G3BP1 (Fig. 3i and Extended Data Fig. 9c). We observed a significant reduction in both FUS<sup>R495X</sup>-positive and G3BP1-positive stress granules in cells treated with **5** (Fig. 3j). Treatment with **5** led to more substantial reductions in stress granules than simultaneous treatment with both

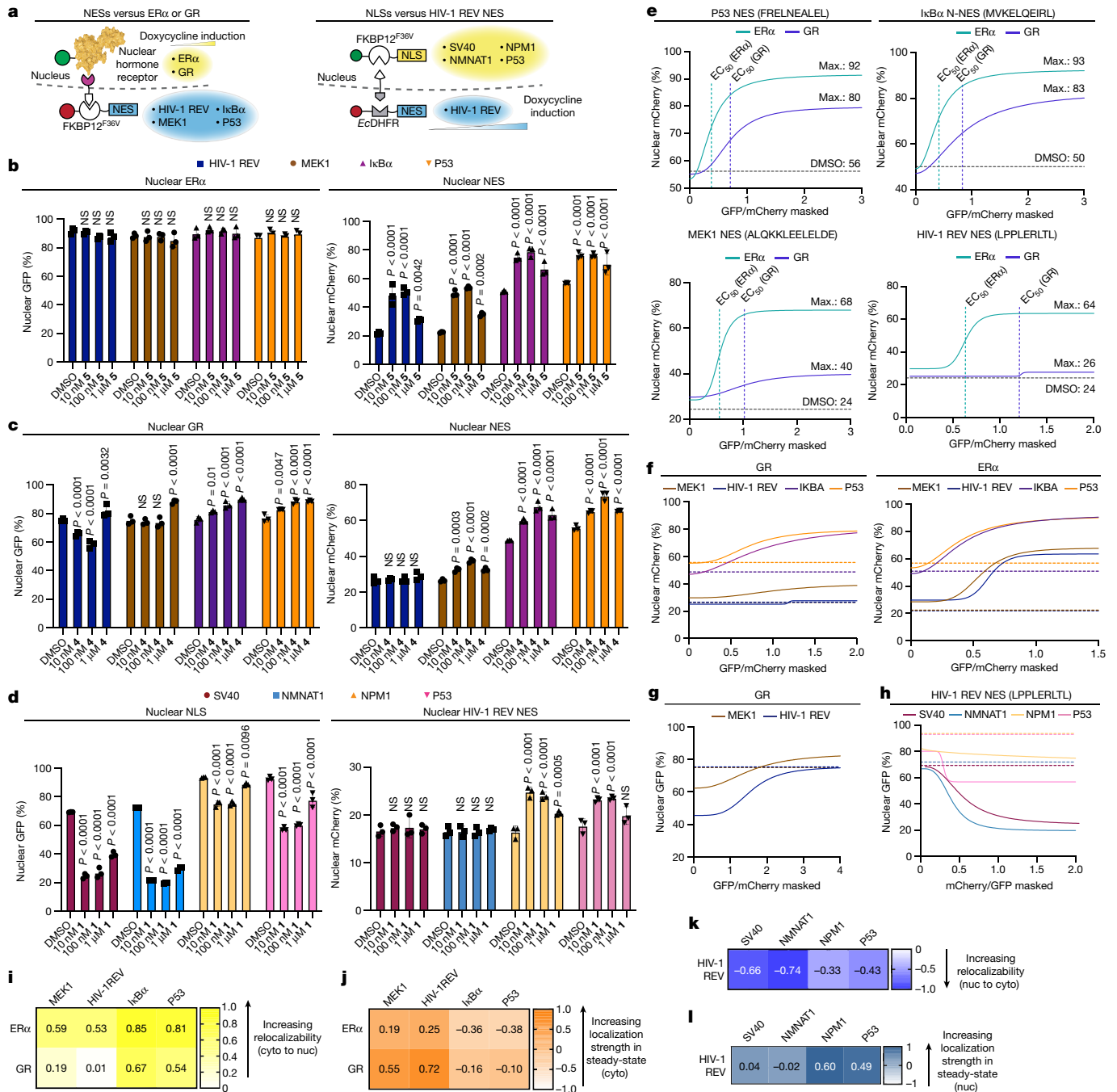


**Fig. 2 | Nuclear hormone receptors are shuttles for cytoplasmic and diffuse proteins and provide a basis for quantitative assessment of target relocalization susceptibility.** **a**, Combinatorial pairing of GR or ER $\alpha$  with NESs, and HIV-1REV NES with NLSs. **b,c**, Quantification of the mean percentage nuclear fluorophore in HeLa cells expressing ER $\alpha$  (**b**) or GR (**c**) and the NES sequences at different doses of **5** or **4**, respectively, after 3 h. **d**, Quantification of the mean percentage nuclear fluorophore in HeLa cells expressing HIV-1REV NES and the respective NLS sequences at different doses of **1** after 3 h. **e**, Sigmoidal best-fit curves derived from single-cell plots of the mean percentage nuclear fluorophore against relative GFP/mCherry ratio. Comparison of target NES-bearing protein relocalization into the nucleus by GR or ER $\alpha$  with 100 nM **4** or **5** after 3 h. DMSO treatment is plotted as a dotted line. **f**, Best-fit curves as in **e** comparing targets for each shuttle. **g**, Analysis of GR localization across MEK1

and HIV-1 REV NES. **h**, Comparison of NLS-containing target protein relocalization into the nucleus by HIV-1REV NES at the optimal concentrations of **1** after 3 h (100 nM for SV40, NMNAT1; 10 nM for NPM1, P53). **i**, Relocalizability score of the NES-containing target proteins when partnered with GR or ER $\alpha$ . **j**, Localization score of the NLS-containing target proteins when partnered with GR or ER $\alpha$ . **k**, Relocalizability score of the NLS-containing target proteins when partnered with HIV-1REV NES. **l**, Localization score of the NLS-containing target proteins when partnered with HIV-1REV NES. For **g**, **h** and **h**, DMSO treatment values are shown as a dashed line of the respective colour. Data in **b**, **c** and **d** are mean  $\pm$  s.d. of three independent experiments. Scale bars, 20  $\mu$ m. *P* values in **b**, **c** and **d** were determined by two-way ANOVA with Dunnett's post hoc test comparing each condition with DMSO within each protein pairing. Max., maximum.

## Endogenous protein relocalization

The ability to exploit the cereblon-damaged DNA-binding protein 1 (CRBN-DDB1) and Von Hippel-Lindau (VHL) E3 ligases as general

unlinked warheads **3** and **10** (Fig. 3k,l and Extended Data Fig. 9d). This demonstrates that FUS<sup>R495X</sup> can be relocalized from stress granules to the nucleus and that TRAM treatment can reduce FUS<sup>R495X</sup>-positive and G3BP1-positive granules.

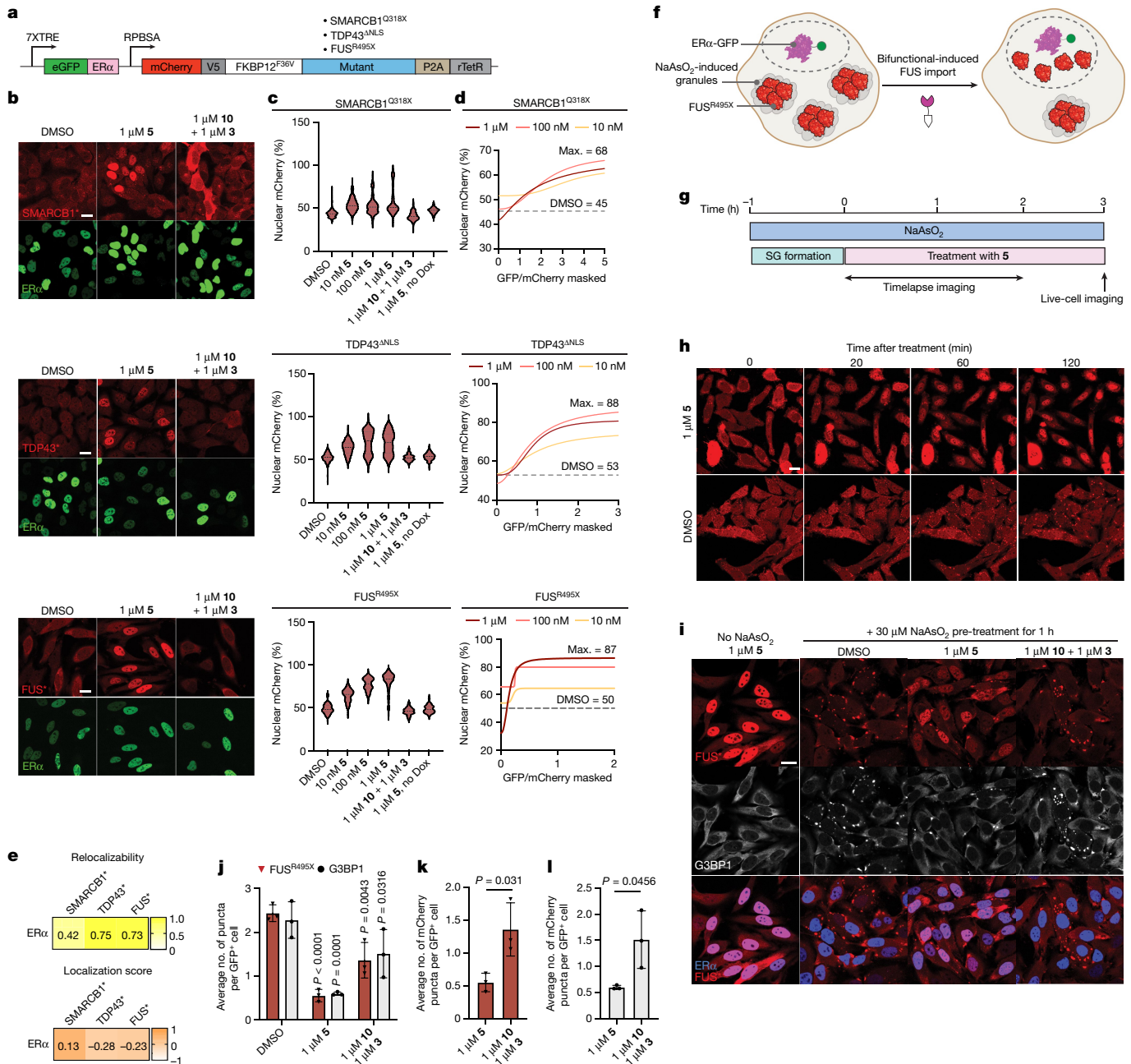


**Fig. 3 | Targeted relocalization can move mutant proteins into nuclei and out of stress granules.** **a**, Genetic constructs for stable incorporation. **b**, Representative images of HeLa cells stably expressing the target proteins SMARCB1<sup>Q318X</sup>, TDP43<sup>ΔNLS</sup> (TDP43<sup>(K52A/R85A/K84A)</sup>) or FUS<sup>R495X</sup> and shuttle protein ER $\alpha$  under an inducible promoter after 3 h of treatment with **5**. **c**, Representative violin plots of population shifts in percentage nuclear target protein upon treatment with **5** for 3 h. **d**, Best-fit curves derived from single-cell plots of percentage nuclear mCherry against GFP/mCherry. **e**, Relocalizability and localization strengths calculated for SMARCB1<sup>Q318X</sup>, TDP43<sup>ΔNLS</sup> or FUS<sup>R495X</sup> using ER $\alpha$  as a shuttle protein. **f**, Schematic for ER $\alpha$ -induced relocalization of FUS<sup>R495X</sup> from stress granules. **g**, Experimental workflow for cells pre-treated with NaAsO<sub>2</sub> for an hour to induce stress granule formation before relocalization through TRAM treatment. **h**, Timelapse live-cell imaging snapshots of FUS<sup>R495X</sup> extraction from granules after treatment with **5**. **i**, Representative fixed-cell immunofluorescent images of stress granule marker G3BP1 and

mCherry–FUS<sup>R495X</sup> after treatment with **5** or control compounds. **j**, Quantification of stress granules in cells after treatment with **5** or control compounds. **k**, Comparison of mCherry–FUS<sup>R495X</sup>-positive puncta in cells treated with bifunctional molecule **5** or control molecules. **l**, Comparison of G3BP1-positive puncta in cells treated with bifunctional molecule **5** or control molecules. Images in **b** and **h** are representative of three biological replicates. Images in **i** are representative of three biological replicates. Three fields of view totalling a minimum of 40 cells per condition per repeat were used to generate mean values for **j**, **k** and **l**. Data in **j**, **k** and **l** are mean  $\pm$  s.d. of three independent experiments. Violin plots in **c** are representative of three independent experiments. Scale bars, 20  $\mu$ m. *P* values in **j** were determined by two-way ANOVA with Dunnett's post hoc test comparing each dataset with its relative DMSO control. *P* values in **k** and **l** were determined by unpaired two-tailed *t*-tests. SG, stress granule; \* denotes mutation as defined in **a**.

effector proteins with well-characterized small-molecule warheads has contributed to the rapid advancement of targeted protein degradation. We sought similarly general shuttle proteins that are expressed

at high levels in most cell types. We identified METAP2 as a suitable nuclear export shuttle, and PARP1 as a nuclear import shuttle with well-characterized warheads. To demonstrate that these proteins could

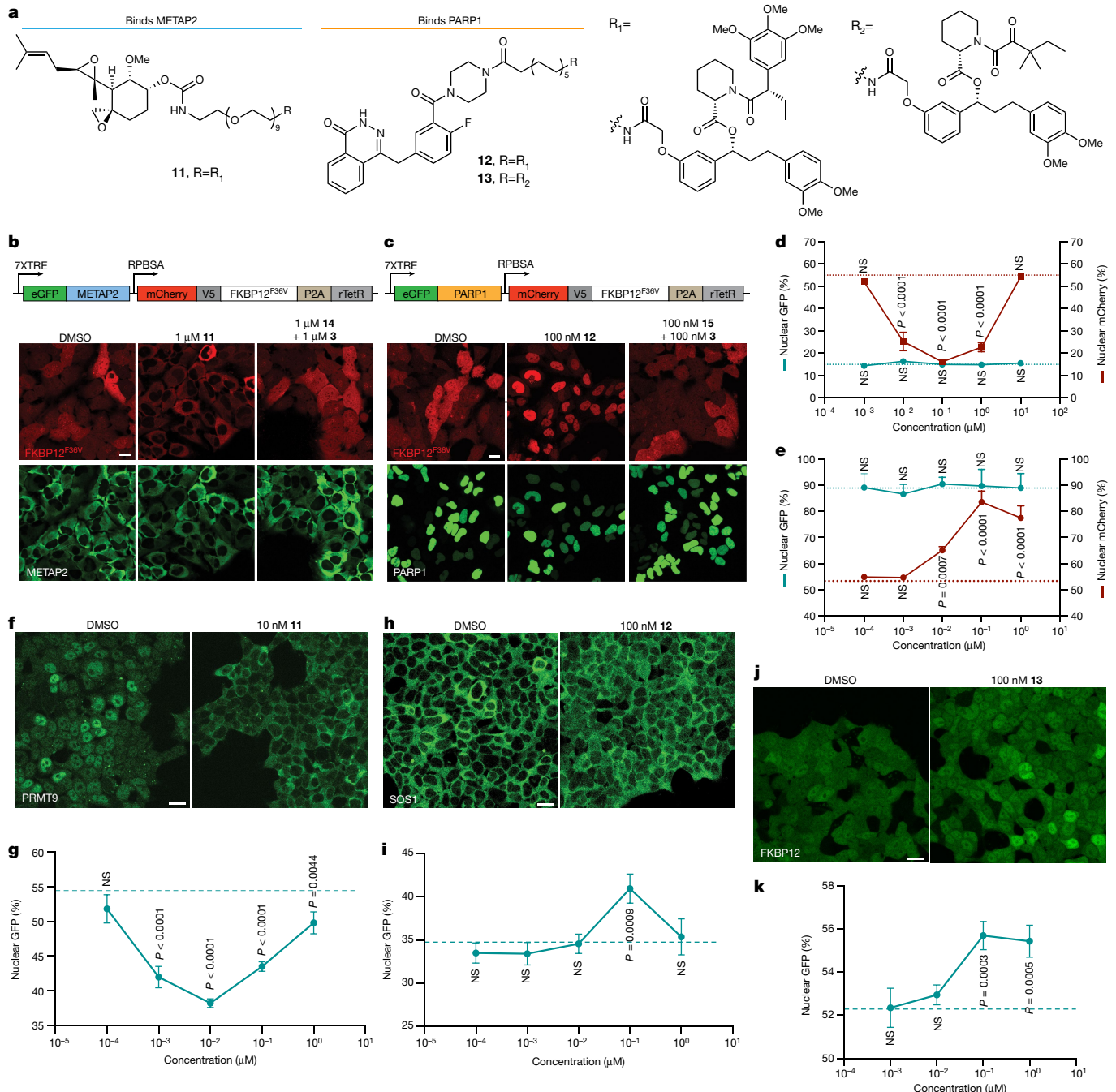


**Fig. 4 | Endogenous targets are susceptible to relocalization with TRAMs that engage endogenous shuttles.** **a**, Bifunctional molecules that engage METAP2 or PARP1 and FKBP12<sup>F36V</sup> or FKBP12. **b**, Representative live-cell images of FKBP12<sup>F36V</sup> nuclear export when treated with **11** or unlinked warhead controls for 3 h. **c**, Representative live-cell images of FKBP12<sup>F36V</sup> nuclear import when treated with **12** or unlinked warhead controls for 3 h. **d**, Dose–response curve for percentage of nuclear FKBP12<sup>F36V</sup> after a 3 h of treatment with **11**. **e**, Dose–response curve for percentage of nuclear FKBP12<sup>F36V</sup> after a 3 h treatment with **12**. **f**, Representative live-cell images of PRMT9 knock-in HEK293T cells treated for 24 h with **11**. **g**, Dose–response curve for percentage of nuclear

PRMT9 after a 24 h treatment with **11**. **h**, Representative live-cell images of SOS1 knock-in HEK293T cells treated for 24 h with **12**. **i**, Dose–response curve for percentage of nuclear SOS1 after a 24 h treatment with **12**. **j**, Representative live-cell images of FKBP12 knock-in HEK293T cells treated for 24 h with **13**. **k**, Dose–response curve for percentage of nuclear FKBP12 after a 24 h treatment with **13**. Images in **b**, **c**, **f**, **h** and **j** are representative of three biological replicates. Data in **d**, **e**, **g**, **i** and **k** are mean  $\pm$  s.d. of three independent experiments. *P* values in **d**, **e**, **g**, **i** and **k** were determined by one-way ANOVA with Dunnett's post hoc test comparing each condition with the DMSO control. Scale bars, 20  $\mu$ m.

be used as suitable shuttles, we synthesized **11**–**13** (Fig. 4a), which use fumagillo-l- and olaparib-based warheads to engage METAP2 and PARP1, respectively. Using ectopically expressed model constructs, we validated that TRAMs **11** and **12** are able to engage METAP2 and PARP1 to nuclear exclude or enhance FKBP12<sup>F36V</sup>, respectively, and that ternary complex formation is necessary for this relocalization (Fig. 4b,c and

Extended Data Fig. 10). We observed dose-dependent relocalization that reached a minimum of 12% nuclear localization by using **11** to engage METAP2 (Fig. 4d) and a maximum of 84% nuclear localization by using **12** to engage PARP1 (Fig. 4e).

The examination of targeted relocalization of endogenous proteins as a therapeutic approach is limited by a lack of small-molecule ligands

for any desired target protein. To bypass this challenge, we used a modified Cas9-based protocol for microhomology-mediated end joining to install binding domains and fluorescent proteins on endogenous protein targets (Extended Data Fig. 11). We designed a guide RNA plasmid with two orthogonal U6 promoters and stem loops to facilitate rapid cloning for knock-in onto different targets. To illustrate endogenous protein relocalization using endogenously expressed shuttle proteins, we sought candidate targets that had undergone successful tagging in the OpenCell database<sup>43</sup>. PRMT9 is a nuclear-enhanced protein that has recently been explored as a target in acute myeloid leukaemia<sup>44</sup>. Using CRISPR–Cas9 tagging, we inserted a GFP–FKBP12<sup>F36V</sup> cassette onto PRMT9, and demonstrated that we could nuclear exclude PRMT9 upon treatment with TRAM 11, which engages endogenous METAP2 as an export shuttle. Dose-dependent relocalization was observed for the export of endogenous PRMT9 by endogenous METAP2, with maximum export observed at 10 nM of 11 (Fig. 4f,g and Extended Data Fig. 12a,b). Nuclear export with TRAM 11 was not observed when cells were treated with unlinked warheads 3 and 14 (Extended Data Fig. 12c–e). Pre-treatment with 14 or competitive treatment with 3 mitigated the observed nuclear export (Extended Data Fig. 12f,g), illustrating the dependence of relocalization on effective ternary complex formation. To study endogenous protein nuclear import, we appended the GFP–FKBP12<sup>F36V</sup> cassette onto endogenous SOS1, which is known to have strong cytoplasmic localization and membrane association. Treatment with TRAM 12 engaging PARP1 resulted in partial redistribution of SOS1 from the cytoplasm to the nucleus (Fig. 4h,i and Extended Data Fig. 13a,b), which was not observed when treated with the unlinked warheads and was abolished when competed with unlinked warheads 15 or 3 (Extended Data Fig. 13c–g).

Motivated by the finding that endogenous levels of shuttle proteins were sufficient to relocalize endogenous protein targets, we synthesized TRAM 13 from warheads directly engaging endogenous FKBP12 and PARP1 and inserted GFP onto endogenous FKBP12 for live-cell visualization. Upon treatment with TRAM 13, significant nuclear enhancement of FKBP12 was observed (Fig. 4j,k and Extended Data Fig. 14a,b), which was abolished upon co-treatment or competition with the unlinked warheads (Extended Data Fig. 14c–g). Here we showcase relocalization of a protein by a rationally designed bifunctional molecule that directly engages both endogenous shuttle and target proteins. Across all three endogenous protein relocalization examples, a homogenous population shift was observed upon TRAM treatment, unlike the ectopic expression models for which relocalization is often observed in a subset of the cell population. This suggests that the minimum relative shuttle protein-to-target protein ratio requirement can be achieved throughout the population in endogenous systems.

### NMNAT1 relocalization slows axonal degeneration

Targeted protein relocalization by means of coupling to a shuttle protein could enable pharmacological approaches that mimic beneficial gain-of-function mutations. WldS, a mutant protein consisting of mouse NMNAT1 (mNMNAT1) fused to a truncated N-terminal region of UBE4B, has been shown to be protective against Wallerian neurodegeneration<sup>45–47</sup>. Mice bearing the WldS mutation have shown increased resistance to neuropathies and ALS<sup>48,49</sup>. The ability for small amounts of WldS to traffic to the axon is crucial for its protective function, where it serves to maintain the levels of NAD<sup>+</sup> upon loss of axonal nicotinamide nucleotide adenyllyltransferase 2 (NMNAT2) during early stages of axonal injury<sup>50</sup>. We reasoned that small-molecule-mediated transport of NMNAT1 from the nucleus down the axon might serve a similar function to WldS and provide a proof-of-concept example for protein relocalization to drive a gain-of-function phenotype. We collected dorsal root ganglion (DRG) neurons from rat embryos and transduced them with adeno-associated viruses (AAVs) expressing mNMNAT1 linked to FKBP12<sup>F36V</sup> and a truncated sequence of axon-localized GAP-43, fused

to EcDHFR (Fig. 5a,b). When we treated these neurons with 1, clear redistribution of mNMNAT1 down axons was observed, which did not occur when neurons were co-treated with unlinked warheads 2 and 3 (Fig. 5c and Extended Data Fig. 15a). To assess the protective function of mNMNAT1 relocalization, after treatment with 1, we performed an axotomy and removed the cell bodies (Extended Data Fig. 15b). We observed persistent mNMNAT1 expression in axons post-axotomy only in neurons treated with TRAM 1. Distinct blebbing and fragmentation of neurites was observed in dimethylsulfoxide (DMSO) or unlinked warhead co-treated neurons 24 h after axotomy, with near complete neurite death observed after 48 h (Fig. 5d, Extended Data Fig. 15c and Supplementary Fig. 6). However, in neurons treated with 1, both axon health and axon termini health were maintained for at least 72 h after axotomy and attenuated axon death was observed only after 96 h (Fig. 5d–f and Extended Data Fig. 15d–g). These observations are consistent with a gain-of-function protective activity of NMNAT1 driven by targeted, TRAM-mediated relocalization from nuclei to axons.

### Discussion

Subcellular protein localization often serves as a control mechanism for protein activity, and alterations in a protein's localization can form the basis of numerous diseases. Controlling protein location by hijacking the transport mechanisms of another protein could serve as a therapeutic approach for precision manipulation of protein function. In the present study, we have developed a quantitative single-cell analysis approach to examine the potential for TRAM-mediated coupling of a target protein with a shuttle protein. We have shown that the relative expression levels of the two protein partners is a predominant parameter in driving the ability to relocalize a target protein. We have also demonstrated that the localization of an endogenous target protein can be overturned by a coupling to an endogenous shuttle protein. Pioneering work using chemical methods to influence nucleocytoplasmic transport has relied on pitting two synthetic localization signals against each other<sup>25</sup>. Extending these efforts to native systems, as we have done here, represents the next frontier in controlling mammalian protein localization pharmacologically. Quantification of relative localization strength between proteins remains an open challenge<sup>51</sup>, with context dependencies that are probably intrinsic to each individual protein. Quantitative analysis at the single-cell level is essential for assessing the ability for small molecules to coopt other mammalian machinery. Here we develop and deploy a relocalizability metric as well as a relative localization strength metric which might serve as a basis for further comparisons. These metrics could inform the rational choice of protein partners for programmable degrees of target protein relocalization.

Tethering two proteins together to alter the trafficking of one partner necessitates suitable shuttle proteins with ligands. Nuclear hormone receptors are common targets for small-molecule therapeutics and exhibit nuclear translocation or localization. We have developed molecules that employ binders of nuclear hormone receptors and can harness them to drive enrichment of a protein target in the nucleus. Using discrete shuttles that are differentially expressed in disease contexts such as cancer or are uniquely expressed in certain cell types enables the future prospect of targeted relocalization-based therapies that can generate beneficial phenotypic consequences. The mislocalization of transcriptional regulators or RNA-binding proteins has been observed in cancers and neurodegenerative diseases. Mutations that truncate or impair NLSS are particularly pathogenic, with no clear mechanism for therapeutic intervention beyond genetic manipulation. We demonstrate the ability of small-molecule-mediated targeted relocalization using nuclear hormone receptors to return these proteins to the nucleus from the cytoplasm or stress granules. Our data suggest that the redistribution of mislocalized proteins that form the core of stress granules back to nuclei might dissipate these granules.

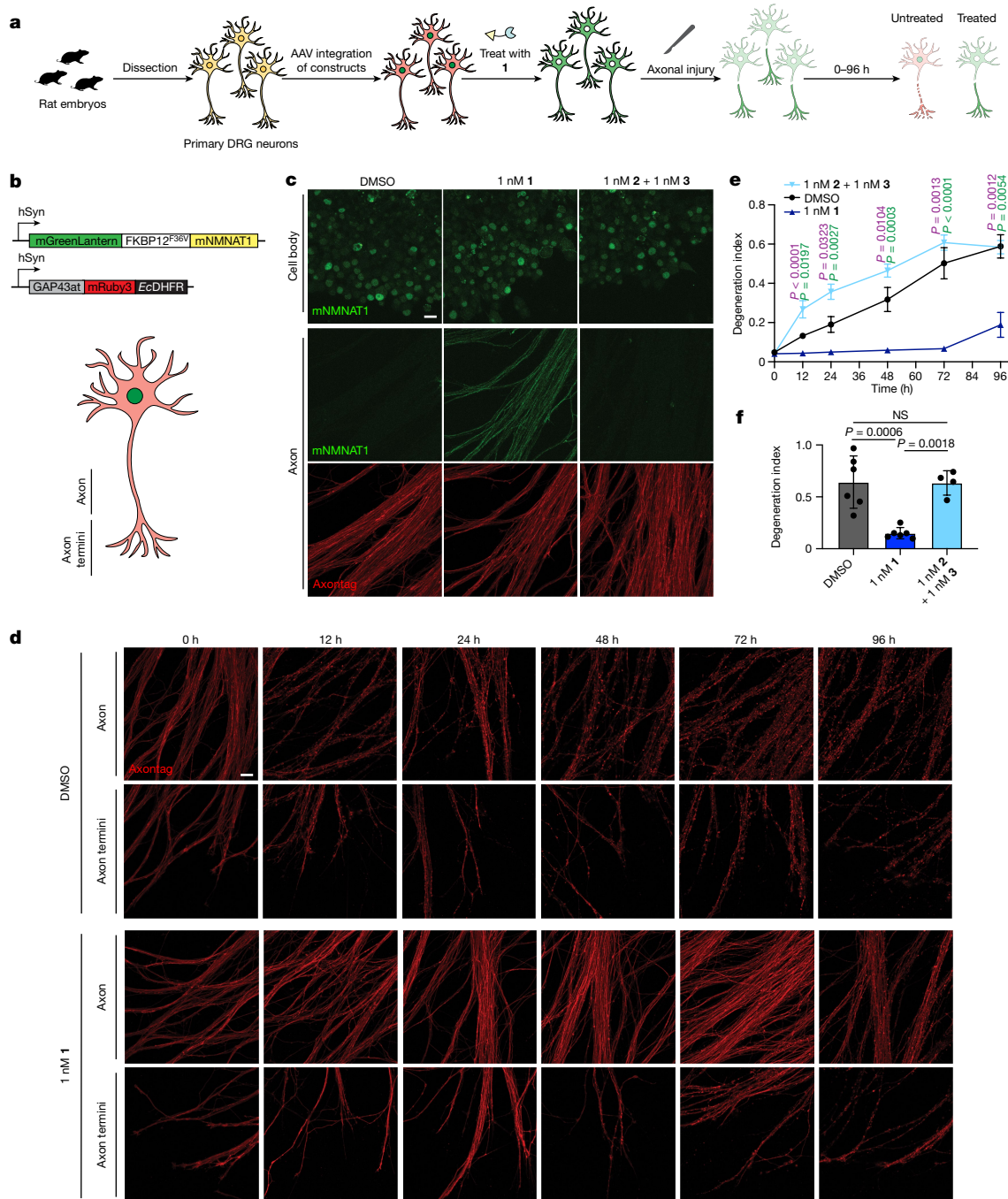


**Fig. 5 | Targeted relocation of NMNAT1 can protect against axon injury.** **a**, Schematic for DRG neuron collection, transduction of model proteins through AAV, small-molecule treatment and axotomy. **b**, Constructs delivered by AAV to study the gain-of-function potential for mNMNAT1 relocalization in neurons, and definition of labels for neuronal imaging. GAP43at is the 20-amino-acid dipalmitoylation domain (MLCCMRRTKQVEKNDEDQKI) found at the N terminus of growth-associated protein-43. **c**, Representative live-cell images of mNMNAT1 in primary DRG neurons when treated with 1 or control molecules. **d**, Representative live-cell images of axonal-tagged protein in axons and axon termini after exposure to 1 for 24 h followed by axotomy to induce degeneration. mRuby3 signal was used to monitor degeneration across treated neurons. AxonTag, GAP43at-mRuby3-EcDHFR. **e**, Quantification of axonal

degeneration over time in the axon. **f**, Quantification of degeneration at 72 h of axon termini. Images in **c** and **d** are representative of neurons collected from four embryos. For the plots in **e**, three replicates each from four embryos were combined for DMSO and 1 nM 1; for the 1 nM 2 + 1 nM 3 condition, three replicates each from two embryos were combined. For plots in **f**, a total of six replicates derived from four different embryos were combined for the DMSO and 1 nM 1 treatment data, and a total of four replicates derived from two different embryos were combined for the 1 nM 2 + 1 nM 3 condition. Data in **e** and **f** are mean  $\pm$  s.e.m. *P* values in **e** and **f** were determined by two-way ANOVA with Tukey's post hoc test comparing the 1 nM treatment of 1 with the DMSO (purple) or the unlinked warhead control (green) at each time point. Scale bars, 20  $\mu$ m.

Targeted redistribution of endogenous proteins driven by small molecules has been challenging to rigorously demonstrate in live cells, necessitating methods for analysing protein localization quantitatively with high sensitivity. Small-molecule ligands to engage shuttles

of the requisite expression level and localization strengths must be paired with ligands for target proteins. Genetic tagging of endogenous proteins with ligand-binding domains has been transformative to study targets for protein degradation with universal small molecules.

# Article

We show, by means of endogenous knock-in of binding domains, the ability to redistribute endogenous proteins using METAP2 or PARP1 as general nuclear export or import shuttles, respectively. We further demonstrate the utility of sensitive imaging analyses to report on the redistribution of endogenous, highly expressed FKBP12 using endogenous PARP1 with a TRAM directly engaging both proteins. The degrees of relocalization of SOS1 and FKBP12 were smaller (less than 10%) than that observed for PRMT9. These experiments demonstrate that strongly localized or highly abundant proteins can undergo TRAM-mediated relocalization, albeit to a small degree. The critical amount of relocalization needed to confer a biological phenotype is likely to be target dependent. Our work establishes that targeted relocalization of endogenous proteins is possible, and further work is needed to define the extents necessary for gain-of-function phenotypes in endogenous systems. The endogenous proteins examined exhibit population-wide redistribution as a function of TRAM treatment. The structure of linkers within bivalent molecules can often be a key parameter for efficacy in PTM-targeting induced proximity approaches. Our efforts with PARP1 and METAP2 were supported by previously published studies describing effective linking strategies<sup>52,53</sup>. Further exploration of linking strategies of target and shuttle binding warheads for any protein pair might reveal cooperative binding events for highly effective TRAMs.

An attractive aspect of targeted protein relocalization is the ability to impart protein function in a new subcellular compartment. The WldS mutation has been extensively studied for its ability to confer protection against neurodegenerative conditions. A consensus protective function of WldS is maintaining the balance of NAD<sup>+</sup> in axons during injury. Small-molecule approaches to target this axis have attempted to inhibit the widely expressed NADase enzyme SARM1 (refs. 54,55). Targeted relocalization of NMNAT1 might serve to compensate for the loss of NMNAT2 during early neurodegeneration and could present an alternative approach amenable to specific targeting using neuron-specific transport pathways. We demonstrate protection from axonal degeneration by partial relocalization of NMNAT1 from nuclei down axons induced by TRAMs.

In this demonstration, TRAMs bind concurrently to a target protein and shuttle protein and confer relocalization in a stoichiometric mechanism of action. This limitation is not observed with bifunctional degraders and other PTM modifier-recruiting molecules, which benefit from event-driven or sub-stoichiometric mechanisms. The stoichiometric mode of action of TRAMs also requires higher expression of a shuttle protein compared with a target protein, which might limit the scope of potential targets for relocalization. Recent reports combine occupancy-driven mechanisms that operate by means of stoichiometric target engagement with downstream amplified phenotypic consequences<sup>34</sup>. In principle, movement of a target protein to a new subcellular location could enable numerous mechanisms for rewiring cellular activity. Neosubstrates of enzymes might be accessible entirely through TRAM-induced relocalization. Relocalization of mislocalized transcription factors or RNA-binding proteins might similarly restore substrate accessibility. To realize these ideas, further work on the extent of relocalization required to observe different phenotypes will be essential. As most warheads used for bifunctional molecule development are inhibitors, available ligands might not be suitable to fully realize the potential of TRAMs due to inhibition of effector functions. Whether a target protein can perform functions while tethered to a shuttle remains an important question for each new system. Medicinal chemistry campaigns can bridge these gaps by developing non-inhibitory binders of target proteins to facilitate gain-of-function phenotypes upon relocalization. To do so will require identification of appropriate targets and shuttles for a desired phenotype. Choices of targets and shuttle pairings can be informed through relative relocalizability metrics defined for a larger set of proteins. Insights into features governing relocalizability will

further enhance therapeutic efforts. Combined with non-inhibitory molecule development, interactome rewiring by means of protein localization manipulation has the potential to contribute to advances in both fundamental biology and development of next-generation therapeutics.

## Online content

Any methods, additional references, Nature Portfolio reporting summaries, source data, extended data, supplementary information, acknowledgements, peer review information; details of author contributions and competing interests; and statements of data and code availability are available at <https://doi.org/10.1038/s41586-024-07950-8>.

1. Kau, T. R., Way, J. C. & Silver, P. A. Nuclear transport and cancer: from mechanism to intervention. *Nat. Rev. Cancer* **4**, 106–117 (2004).
2. Suk, T. R. & Rousseau, M. W. C. The role of TDP-43 mislocalization in amyotrophic lateral sclerosis. *Mol. Neurodegener.* **15**, 45 (2020).
3. Hung, M.-C. & Link, W. Protein localization in disease and therapy. *J. Cell Sci.* **124**, 3381–3392 (2011).
4. Krauss, R., Bosanac, T., Devraj, R., Engber, T. & Hughes, R. O. Axons matter: the promise of treating neurodegenerative disorders by targeting SARM1-mediated axonal degeneration. *Trends Pharmacol. Sci.* **41**, 281–293 (2020).
5. Thul, P. J. et al. A subcellular map of the human proteome. *Science* **356**, eaal3321 (2017).
6. Wang, X. & Li, S. Protein mislocalization: mechanisms, functions and clinical applications in cancer. *Biochim. Biophys. Acta* **1846**, 13–25 (2014).
7. Hill, R., Cautain, B., de Pedro, N. & Link, W. Targeting nucleocytoplasmic transport in cancer therapy. *Oncotarget* **5**, 11–28 (2013).
8. Pasha, T. et al. Karyopherin abnormalities in neurodegenerative proteinopathies. *Brain* **144**, 2915–2932 (2021).
9. Yu, Y. et al. Pathogenic mutations in the ALS gene CCNF cause cytoplasmic mislocalization of Cyclin F and elevated VCP ATPase activity. *Hum. Mol. Genet.* **28**, 3486–3497 (2019).
10. Chou, C.-C. et al. TDP-43 pathology disrupts nuclear pore complexes and nucleocytoplasmic transport in ALS/FTD. *Nat. Neurosci.* **21**, 228–239 (2018).
11. Birsa, N., Bentham, M. P. & Fratta, P. Cytoplasmic functions of TDP-43 and FUS and their role in ALS. *Semin. Cell Dev. Biol.* **99**, 193–201 (2020).
12. Vance, C. et al. ALS mutant FUS disrupts nuclear localization and sequesters wild-type FUS within cytoplasmic stress granules. *Hum. Mol. Genet.* **22**, 2676–2688 (2013).
13. Wang, A. Y. & Liu, H. The past, present, and future of CRM1/XPO1 inhibitors. *Stern Cell Investig.* **6**, 6 (2019).
14. Jans, D. A., Martin, A. J. & Wagstaff, K. M. Inhibitors of nuclear transport. *Curr. Opin. Cell Biol.* **58**, 50–60 (2019).
15. Syed, Y. Y. Selinexor: first global approval. *Drugs* **79**, 1485–1494 (2019).
16. Abdul Razak, A. R. et al. First-in-class, first-in-human phase I study of selinexor, a selective inhibitor of nuclear export, in patients with advanced solid tumors. *J. Clin. Oncol.* **34**, 4142–4150 (2016).
17. Griffith, M. et al. DGIdb: mining the druggable genome. *Nat. Methods* **10**, 1209–1210 (2013).
18. Cromm, P. M. & Crews, C. M. Targeted protein degradation: from chemical biology to drug discovery. *Cell Chem. Biol.* **24**, 1181–1190 (2017).
19. Burslem, G. M. & Crews, C. M. Small-molecule modulation of protein homeostasis. *Chem. Rev.* **117**, 11269–11301 (2017).
20. Kanwal, C., Mu, S., Kern, S. E. & Lim, C. S. Bidirectional on/off switch for controlled targeting of proteins to subcellular compartments. *J. Control. Release* **98**, 379–393 (2004).
21. Dixon, A. S., Constance, J. E., Tanaka, T., Rabbits, T. H. & Lim, C. S. Changing the subcellular location of the oncprotein Bcr-Abl using rationally designed capture motifs. *Pharm. Res.* **29**, 1098–1109 (2012).
22. Niopek, D. et al. Engineering light-inducible nuclear localization signals for precise spatiotemporal control of protein dynamics in living cells. *Nat. Commun.* **5**, 4404 (2014).
23. Yumerefendi, H. et al. Light-induced nuclear export reveals rapid dynamics of epigenetic modifications. *Nat. Chem. Biol.* **12**, 399–401 (2016).
24. Jayanthi, B., Bachhav, B., Wan, Z., Martinez Legaspi, S. & Segatori, L. A platform for post-translational spatiotemporal control of cellular proteins. *Synth. Biol. (Oxf.)* **6**, ysab002 (2021).
25. Klemm, J. D., Beals, C. R. & Crabtree, G. R. Rapid targeting of nuclear proteins to the cytoplasm. *Curr. Biol.* **7**, 638–644 (1997).
26. Geda, P. et al. A small molecule-directed approach to control protein localization and function. *Yeast* **25**, 577–594 (2008).
27. Raschbichler, V., Lieber, D. & Bailer, S. M. NEX-TRAP, a novel method for in vivo analysis of nuclear export of proteins. *Traffic* **13**, 1326–1334 (2012).
28. Robinson, M. S., Sahlen, D. A. & Foster, S. D. Rapid inactivation of proteins by rapamycin-induced rerouting to mitochondria. *Dev. Cell* **18**, 324–331 (2010).
29. Ishida, M. et al. Synthetic self-localizing ligands that control the spatial location of proteins in living cells. *J. Am. Chem. Soc.* **135**, 12684–12689 (2013).
30. Nakamura, A. et al. Chemogenetic control of protein anchoring to endomembranes in living cells with lipid-tethered small molecules. *Biochemistry* **59**, 205–211 (2020).
31. Wing, C. E., Fung, H. Y. J. & Chook, Y. M. Karyopherin-mediated nucleocytoplasmic transport. *Nat. Rev. Mol. Cell Biol.* **23**, 307–328 (2022).
32. Love, D. C., Sweitzer, T. D. & Hanover, J. A. Reconstitution of HIV-1 Rev nuclear export: independent requirements for nuclear import and export. *Proc. Natl. Acad. Sci. USA* **95**, 10608–10613 (1998).

33. Gibson, T. J., Seiler, M. & Veitia, R. A. The transience of transient overexpression. *Nat. Methods* **10**, 715–721 (2013).
34. Gourisankar, S. et al. Rewiring cancer drivers to activate apoptosis. *Nature* **620**, 417–425 (2023).
35. Højfeldt, J. W. et al. Bifunctional ligands allow deliberate extrinsic reprogramming of the glucocorticoid receptor. *Mol. Endocrinol.* **28**, 249–259 (2014).
36. Gallagher, S. S., Miller, L. W. & Cornish, V. W. An orthogonal dexamethasone-trimethoprim yeast three-hybrid system. *Anal. Biochem.* **363**, 160–162 (2007).
37. Gazorpak, M. et al. Harnessing PROTAC technology to combat stress hormone receptor activation. *Nat. Commun.* **14**, 8177 (2023).
38. Pathak, R. et al. Inhibition of nuclear export restores nuclear localization and residual tumor suppressor function of truncated SMARCB1/INI1 protein in a molecular subset of atypical teratoid/rhabdoid tumors. *Acta Neuropathol.* **142**, 361–374 (2021).
39. de Boer, E. M. J. et al. TDP-43 proteinopathies: a new wave of neurodegenerative diseases. *J. Neurol. Neurosurg. Psychiatry* **92**, 86–95 (2020).
40. Dormann, D. et al. ALS-associated fused in sarcoma (FUS) mutations disrupt Transportin-mediated nuclear import. *EMBO J.* **29**, 2841–2857 (2010).
41. Waibel, S., Neumann, M., Rabe, M., Meyer, T. & Ludolph, A. C. Novel missense and truncating mutations in FUS/TLS in familial ALS. *Neurology* **75**, 815–817 (2010).
42. Bosco, D. A. et al. Mutant FUS proteins that cause amyotrophic lateral sclerosis incorporate into stress granules. *Hum. Mol. Genet.* **19**, 4160–4175 (2010).
43. Cho, N. H. et al. OpenCell: endogenous tagging for the cartography of human cellular organization. *Science* **375**, eabi6983 (2022).
44. Dong, H. et al. Targeting PRMT9-mediated arginine methylation suppresses cancer stem cell maintenance and elicits cGAS-mediated anticancer immunity. *Nat. Cancer* **5**, 601–624 (2024).
45. Coleman, M. P. & Freeman, M. R. Wallerian degeneration, WldS, and Nmnat. *Annu. Rev. Neurosci.* **33**, 245–267 (2010).
46. Conforti, L. et al. Wld S protein requires Nmnat activity and a short N-terminal sequence to protect axons in mice. *J. Cell Biol.* **184**, 491–500 (2009).
47. Babetto, E. et al. Targeting NMNAT1 to axons and synapses transforms its neuroprotective potency in vivo. *J. Neurosci.* **30**, 13291–13304 (2010).
48. Fischer, L. R. et al. The *WldS* gene modestly prolongs survival in the SOD1G93A fALS mouse. *Neurobiol. Dis.* **19**, 293–300 (2005).
49. Wang, M. S. et al. The *WldS* protein protects against axonal degeneration: a model of gene therapy for peripheral neuropathy. *Ann. Neurol.* **50**, 773–779 (2001).
50. Wang, J. T., Medress, Z. A., Vargas, M. E. & Barres, B. A. Local axonal protection by *WldS* as revealed by conditional regulation of protein stability. *Proc. Natl Acad. Sci. USA* **112**, 10093–10100 (2015).
51. Henderson, B. R. & Eleftheriou, A. A comparison of the activity, sequence specificity, and CRM1-dependence of different nuclear export signals. *Exp. Cell. Res.* **256**, 213–224 (2000).
52. Cao, C. et al. Discovery of SK-575 as a highly potent and efficacious proteolysis-targeting chimera degrader of PARP1 for treating cancers. *J. Med. Chem.* **63**, 11012–11033 (2020).
53. Zhou, G.-C. et al. Design, synthesis and evaluation of a cellular stable and detectable biotinylated fumagillin probe and investigation of cell permeability of fumagillin and its analogs to endothelial and cancer cells. *Eur. J. Med. Chem.* **70**, 631–639 (2013).
54. Hughes, R. O. et al. Small molecule SARM1 inhibitors recapitulate the SARM1<sup>−/−</sup> phenotype and allow recovery of a metastable pool of axons fated to degenerate. *Cell Rep.* **34**, 108588 (2021).
55. Feldman, H. C. et al. Selective inhibitors of SARM1 targeting an allosteric cysteine in the autoregulatory ARM domain. *Proc. Natl Acad. Sci. USA* **119**, e2208457119 (2022).

**Publisher's note** Springer Nature remains neutral with regard to jurisdictional claims in published maps and institutional affiliations.

Springer Nature or its licensor (e.g. a society or other partner) holds exclusive rights to this article under a publishing agreement with the author(s) or other rightsholder(s); author self-archiving of the accepted manuscript version of this article is solely governed by the terms of such publishing agreement and applicable law.

© The Author(s), under exclusive licence to Springer Nature Limited 2024

## Methods

### Cell lines

Adherent cells were cultured in 10 or 15 cm plates at 37 °C in a 5% CO<sub>2</sub> humidified atmosphere. HeLa and HEK293T cells were obtained from ATCC and were cultured in DMEM supplemented with 10% heat-inactivated fetal bovine serum and 1% penicillin/streptomycin.

### Stable cell line generation with Sleeping Beauty transposase

Fusion protein constructs were cloned into a pSBtet vector flanked by Sleeping Beauty transposase recognition sites which also encoded constitutive expression of the puromycin resistance gene. The day before transfection, 300,000 cells were seeded into a six-well plate. The next day, 1.9 µg of transgene DNA was mixed with 0.1 µg of Sleeping Beauty transposase encoding plasmid in 200 µl of JetPrime buffer, then 4 µl of JetPrime reagent was added. The mixture was gently mixed and left to incubate for 10 min at room temperature, after which it was added dropwise to the well. The next morning, medium was replaced with fresh cell culture medium. Then, 3 d after transfection, antibiotic selection was initiated with 1 µg ml<sup>-1</sup> puromycin until all control cells had died.

### Retrovirus generation

At 1 d before transfection, 1.5 million HEK293T cells were seeded into 6 cm dishes. The following day, 130 µl of complete DMEM was added into an Eppendorf tube. Next, 1 µg of transgene cloned into a pMXs vector was added along with 900 ng of the retrovirus pol/gag and 150 ng of VSVg DNA, and gently mixed. PEI (1 mg ml<sup>-1</sup>) was brought to room temperature and gently mixed before adding 6 µl to the DNA mixture. The mixture was gently mixed and incubated for 20 min at room temperature. Medium in the 6 cm dishes was replaced with fresh complete DMEM. After 20 min of incubation, the transfection mixture was added dropwise to the 6 cm plate, then the plate was returned to the incubator. The next morning, medium was removed and replaced with 5 ml of DMEM containing 30% heat-inactivated fetal serum and 1% penicillin/streptomycin and the plate was returned to the incubator. After 36 h, the medium from the 6 cm plate was collected into a 15 ml Falcon tube and centrifuged at 1,000 rpm for 5 min. The supernatant was filtered through a 0.45 µM filter into 300 µl aliquots. Aliquots were stored at -80 °C.

### Generating stable cell lines with retrovirus

On the day of infection, cells were seeded at a density of 2 million cells per well in a six-well plate, and medium was added to the well up to 3 ml total volume. Then, 3 µl of polybrene transfection reagent (EMD Millipore, catalogue no. TR-1003-G) was added to each well. Viral aliquots were thawed at 37 °C, then gently mixed and added to the well. The plate was then centrifuged at 2,200 rpm for 45 min at 37 °C, then returned to the incubator. The next morning, the cells were lifted and transferred into a 10 cm plate. When cells reached 70–80% confluence, antibiotic selection was started with 10 µg ml<sup>-1</sup> blasticidin until control cells died.

### Lentivirus generation

In total, 1.2 million viral HEK293T cells were seeded per well in a six-well plate. The next day, 6 µl of Mirus-LT1 transfection reagent was mixed with 250 µl of Opti-MEM and left to incubate at room temperature for 15 min. Then, 1.5 µg of transgene cloned into the pU6 transfer vector was mixed with 0.1 µg of gag/pol, 0.1 µg of REV, 0.1 µg of TAT and 0.2 µg of VSVg packaging plasmids. The Opti-MEM and Mirus-LT1 mixture was then added to the DNA mixture, mixed and left to incubate at room temperature for 15 min, then added dropwise to wells. The plate was gently swirled to mix, then returned to the incubator. The next morning, medium in the well was replaced. After 36 h, the supernatant was retrieved into 15 ml Falcon tubes. The tubes were spun down at 300g for 5 min, then the supernatant was filtered through a 0.45 µM filter into 300 µl aliquots. Aliquots were stored at -80 °C.

### Generating stable cell lines with lentivirus

In total, 200,000 cells were seeded per well in a 24-well plate. Polybrene was added (EMD Millipore, catalogue no. TR-1003-G) to a final concentration of 8 µg ml<sup>-1</sup> in a total volume of 1 ml in a well of a 24-well plate, then viral aliquots thawed at 37 °C were added dropwise into the well, and the plate was then returned to the incubator. The next day, the medium was replaced. At 48 h after infection, antibiotic selection was started with 1 µg ml<sup>-1</sup> puromycin until the control well died.

### Live-cell confocal microscopy

Adherent cells were plated (35,000 cells per well in an eight-well chamber slide) 1 d before small-molecule treatment. Doxycycline-inducible lines were plated 2 d before small-molecule treatment at half the seeding density. At 1 d before treatment, cells were treated with doxycycline to a final working concentration of 1 µg ml<sup>-1</sup> in 250 µl of complete growth medium. On the day of treatment, wells were gently rinsed with 2 × 300 µl of PBS, then incubated with 250 µl of complete phenol red-free growth medium with small molecules added for the indicated time. After the indicated time, 1 µl of a fresh Hoechst 33342 solution (0.5 µg µl<sup>-1</sup> in PBS) was added directly to the existing medium in each well to achieve a final Hoechst 33342 concentration of 2 µg ml<sup>-1</sup>, and incubated for 10 min. Cells were imaged with a Nikon A1R confocal microscope using a Plan Fluor ×60 oil immersion, 1.30-numerical aperture (NA) objective. The microscope was equipped with a 405 nm violet laser, a 488 nm blue laser, a 561 nm green laser and a 639 nm laser. Images were exported and analysed using the FIJI software package (v.1.53).

### Fixed-cell confocal microscopy

Adherent cells were plated (50,000 cells per well in an eight-well chamber slide) 1 d before the experiment. Cells were then washed three times with DPBS and fixed with 4% paraformaldehyde in PBS for 15 min at room temperature, washed three times and permeabilized with 0.1% Triton for 5 min at room temperature. Cells were blocked in 10% goat serum in PBS for 1 h at room temperature and incubated with primary antibody overnight at 4 °C. Cells were washed with PBS three times, then incubated with secondary antibody and DAPI for 1 h at room temperature. Cells were washed with PBS and imaged with a Nikon A1R confocal microscope using a Plan Fluor ×60 oil immersion, 1.30-NA objective. The microscope was equipped with a 405 nm violet laser, a 488 nm blue laser, a 561 nm green laser and a 639 nm laser. Images were exported and analysed using the FIJI software package (v.1.53).

### Custom imaging analysis pipeline construction

- Segmentation: a binary image is generated from a nuclear-stained image (for example, DAPI) of a field of view using Otsu thresholding. This binary image is then used as a mask to label coordinates within an acquired field of view corresponding to nuclei. Watershed transform is carried out to segment touching nuclei, and individual nuclei within a field of view are assigned with different numerical labels starting from 1 ('nlabels').
- Generating masks: 'Celllabels': 'nlabels' are then expanded by 6 pixels circumferentially to capture cell area. At the same time, 'nlabels' is also expanded by 3 pixels to generate 'expandednlabels'. Cytoplasmic labels ('clabels') are obtained by subtracting the 'expandednlabels' from 'celllabels'. 'Nlabels' is also shrunk by 3 pixels to avoid taking in nuclear boundary measurements for the cytoplasm or nuclear readings. These pixel numbers can also be user defined.
- Gating: Average nuclear stain intensities per area ('avg nuc int') are then tabulated for these individual nuclei, and a histogram is generated. Kernel density estimation is used to generate a probability density function from this histogram. A normal distribution centred around the main peak of the probability density function on the basis of the full-width at half-maximum is then generated and overlayed.

Assuming the population ‘avg nuc int’ follows a normal distribution, the ends of the normal distributions are set as the gate bounds. Any nuclei without ‘avg nuc int’ within the set gate bounds are gated out and labels for those nuclei and their respective cytoplasmic label are dropped to give ‘gatednlabels’ and ‘gatedclabels’. Alternatively, if the user wishes to set fixed values for the gate bounds, this can also be passed in as an argument in the script.

4. Summing intensities per cell: Fluorophore images for this field of view are overlayed with the ‘gatednlabels’ and ‘gatedclabels’ to extract fluorophore intensities tabulated for every single nuclear and cytoplasmic label. Average fluorophore intensities for each nuclei/cytoplasm label are also generated by dividing the intensity over the area of the label, to give a nuclear and cytoplasmic fluorophore concentration (pixel intensity per area) per cell.

$$\text{Avg GFP nuc intensity per label} = \frac{\text{summed GFP intensity of the label}}{\text{area of label}}$$

5. Calculations and output: For each cell, the average fluorophore pixel intensity per area is then used in the following calculation to estimate percentage nuclear fluorophore:

$$\text{Percentage nuc GFP per label} = \frac{\text{avg GFP nuc intensity per label}}{\text{avg GFP nuc intensity per label} + \text{avg GFP cyto intensity per label}}$$

These values, including the average fluorophore intensity per label, are tabulated in a data frame and output to an Excel file with a separate sheet for each condition. A summary of the mean for each value for each condition is also tabulated and output as an Excel sheet. In addition, a folder is also created containing the gating histogram, as well as overlay masks onto the fluorophore images and the segmentation and nuclear masks from the original nuclear stain images for each field of view.

#### **Modified imaging analysis pipeline for relative protein ratio estimation and validation**

The pipeline built as described above was improved by plotting each individual cell label onto the overlay of the masks on the fluorophore images. This facilitates the user to be able to visually inspect the image and correlate the visual analysis of that cell with the pipeline-derived metrics for that cell. Ten cells for a field of view of a treatment condition were manually picked across a range of protein expression levels by visual analysis. For the ten cells in each image, the drawing tool in ImageJ was used to manually demarcate the cell boundary using the cytoplasmic protein fluorophore image. For each demarcated cell area, the raw integrated density of each fluorophore channel was obtained using the ImageJ measure function. For each cell, the relative ratio of the two fluorophores was obtained by dividing the raw integrated density of GFP by the raw integrated density of RFP to give GFP/mCherry for the whole cell.

$$\text{GFP/mCherry whole cell} = \frac{\text{cell raw integrated density (GFP)}}{\text{cell raw integrated density (RFP)}}$$

For each cell analysed by means of manual integration as detailed above, their average fluorophore nuclear intensity and cytoplasmic intensity obtained from the image analysis pipeline were summed to give an estimate of whole cell fluorophore intensity, and a ratio of this value between the two fluorophores was obtained to give the relative protein ratio estimate of GFP/mCherry masked.

$$\text{GFP/mCherry masked} = \frac{\text{avg nuc GFP intensity} + \text{avg cyto GFP intensity}}{\text{avg nuc RFP intensity} + \text{avg cyto RFP intensity}}$$

The estimate of the relative protein ratio calculated from pipeline metrics (GFP/mCherry masked) was plotted against the relative

protein ratio obtained from manual visual integration using ImageJ (GFP/mCherry whole cell), for all ten cells in each condition, for three repeats. Simple linear regression was used to plot the trendline between the two values, and the Pearson correlation coefficient *R* value was calculated for each graph.

#### **Single-cell plots and best-fit curves to extract theoretical maximal relocalizability**

Percentage nuclear fluorophore metrics for each single cell were plotted against the GFP/mCherry masked values calculated from the image analysis pipeline. Data from three repeats were combined into a single plot for each condition and outliers that had GFP/mCherry masked values beyond 3 s.d. away from the mean were gated out. For nuclear import cases, agonist sigmoidal best-fit curves were plotted using the equation of  $y = \text{bottom} + (\frac{x^{\text{HillSlope}}}{x^{\text{HillSlope}} + EC50^{\text{HillSlope}}}) \times (\text{top} - \text{bottom})$ , where EC50 is the half-maximum effective concentration. For nuclear export cases, antagonist sigmoidal best-fit curves were plotted using the equation of  $y = \text{bottom} + (\text{top} - \text{bottom}) / (1 + (IC50/x)^{\text{HillSlope}})$ . The *y* values at which these best-fit curves plateaued were identified as the theoretical maximum relocalization for that condition.

#### **Relative relocalizability and localization metric calculations**

Relocalizability score is taken as the maximum relocalization demonstrated (extracted from the plateau of the best-fit curve) minus the DMSO-treated percentage nuclear fluorophore, over the maximal theoretical possible change in their respective direction of movement. Relocalizability score is on a scale of -1 to 1, where -1 is the most relocalizable nuclear protein moving from the nucleus to cytoplasm, and 1 is the most relocalizable cytoplasmic protein moving from the cytoplasm to the nucleus.

##### **Relocalizability of a cytoplasmic protein**

$$= \frac{\text{theoretical maximal protein \% nuc} - \text{DMSO treated protein \% nuc}}{|\text{100} - \text{DMSO treated protein \% nuc}|}$$

##### **Relocalizability of a nuclear protein**

$$= \frac{\text{theoretical maximal protein \% nuc} - \text{DMSO treated protein \% nuc}}{|\text{0} - \text{DMSO treated protein \% nuc}|}$$

Relative localization score is given by subtracting the absolute value of the relocalizability score from the initial percentage fluorophore in the steady-state primary compartment.

##### **Cytoplasmic localization score**

$$= \text{DMSO treated protein \% cytoplasmic} - |\text{relocalizability score}|$$

##### **Nuclear localization score**

$$= \text{DMSO treated protein \% nuclear} - |\text{relocalizability score}|$$

#### **Flow cytometry**

Adherent cells were lifted with trypsin and transferred into an Eppendorf or conical tube using complete medium. Cells were pelleted at 300g and washed three times with PBS. Cells were resuspended in PBS and analysed on either a BD Accuri C6+ or an LSR II flow cytometer using FACSDiva software (v.8.0). Data were processed using the FlowJo software package (v.10.0).

#### **Endogenous tagging of proteins using modified PITCh**

To facilitate ease of cloning different target single guide RNAs (sgRNAs) into the cassette, a modified all-in-one CRISPR–Cas9 vector was made containing two orthogonal U6 promoter–stem loop pairs from the parental PITCh vector<sup>56</sup>. The PITCh protocol was then followed to insert donor sequences into endogenous targets. Briefly, a day before

# Article

transfection, adherent cells were seeded at a density of 25,000 cells in a 10 cm dish. On the day of transfection, medium was replaced with 7 ml of Opti-MEM. Both 1.2 µg of guide vector (containing target sgRNA, PITCH sgRNA and Cas9) and 0.6 µg of donor vector were added to 500 µl of Opti-MEM in a 1.5 ml tube. To another 1.5 ml tube containing 500 µl of Opti-MEM was added 30 µl of Lipofectamine 2000. Both tubes were gently mixed and left to incubate for 5 min at room temperature. The two solutions were then mixed and incubated for 30 min at room temperature, after which the mixture was added dropwise to the 10 cm plate containing cells. Cells were incubated for 24 h, after which the medium was replaced with 10 ml of complete growth medium. At 72 h after transfection, medium was replaced with complete growth medium containing puromycin ( $1 \mu\text{g ml}^{-1}$ ), and selection continued by replacing medium with fresh complete growth medium supplemented with puromycin every 2 d. After complete death of control cells, puromycin selection was stopped and cells were expanded for immunoblotting.

## Immunoblotting

Cells were lifted with trypsin then washed with PBS three times and lysed with RIPA buffer supplemented with protease inhibitor cocktail (Roche) and 0.1% Benzonase (Millipore-Sigma) on ice for 15 min in 1.5 ml tubes. The lysates were centrifuged at 21,000 $\times g$  for 15 min at 4 °C. The supernatant was collected, and the protein concentration was determined by BCA assay (Pierce). Equal amounts of lysates were loaded onto 4–12% Bis-Tris gel and separated by SDS-PAGE. The gel was then transferred onto a nitrocellulose membrane and blocked with 5% milk in TBS-T for 1 h at room temperature. The membrane was incubated with primary antibody overnight at 4 °C and washed three times with TBS-T. Subsequently, the membrane was incubated with secondary antibody for 1 h at room temperature and washed three times with TBS-T for visualization with an Odyssey CLx Imager (LI-COR).

## Preparation of antibody-crosslinked beads for immunoprecipitation

Immunoprecipitation with crosslinking was adapted from the Pierce Crosslink Magnetic IP/Co-IP Kit (catalogue no. 88805, Thermo Scientific). Beads were prepared by conjugation with mCherry Polyclonal Antibody (catalogue no. PA5-34974, Invitrogen). For each immunoprecipitation reaction, 2 ml of 1× Modified Coupling Buffer was made by diluting 0.1 ml of 20× Coupling Buffer and 0.1 ml of IP Lysis/Wash Buffer with 1.8 ml of ultrapure water. The bottle of Pierce Protein A/G Magnetic Beads was vortexed to obtain a homogeneous suspension from which 25 µl of beads was aliquoted into a microcentrifuge tube. The tube was placed on a magnetic stand to collect the beads for 1 min. Storage solution was removed and discarded before rinsing the beads with 2 × 500 µl of 1× Modified Coupling Buffer. Then, 7.5 µl of anti-mCherry antibody (catalogue no. PA5-34974, Invitrogen) was diluted to a final concentration of 0.5 µg µl<sup>-1</sup> with ultrapure water, 20× Coupling Buffer (diluted 1:20) and IP Lysis/Wash Buffer (diluted 1:20). Next, 100 µl of the prepared antibody solution was added to the beads and incubated on a rotating platform for 15 min at room temperature. Beads were gently mixed every 5–10 min during incubation to ensure that the beads stayed in suspension. The beads were collected with a magnetic stand and the supernatant was removed and discarded. The beads were washed with 1 × 100 µl of 1× Modified Coupling Buffer and 2 × 300 µl of 1× Modified Coupling Buffer. Then, 217 µl of DMSO was added to a fresh tube of disuccinimidyl suberate (DSS) to prepare a 10× solution (25 mM). This stock solution was mixed, then diluted 1:100 in DMSO to give a 0.25 mM DSS solution. Next, 2.5 µl of 20× Coupling Buffer, 4 µl of 0.25 mM DSS and 43.5 µl of ultrapure water were added to the beads and the beads were incubated for 30 min at room temperature on a rotator. The beads were vortexed every 10–15 min during incubation to ensure that the beads stayed in suspension. Beads were collected with a magnetic stand and the supernatant removed. Then, 100 µl of Elution Buffer was added to the beads and gently mixed for 5 min at room temperature on

a rotating platform. Beads were collected with the magnetic stand, and this process was repeated twice more. Finally, 200 µl of cold RIPA lysis buffer was added to the beads and tubes were inverted to mix. Beads were collected with a magnetic stand, and supernatant was removed to yield the antibody-crosslinked beads.

## Co-immunoprecipitations with TRAMs

For mCherry-eDHFR-NES pulldown, antibody-crosslinked beads were incubated with lysate containing 50 µg of protein made up to a total final volume of 200 µl. To this lysate was added TRAM 1 to a final concentration of 100 nM. The solution was rotated overnight at 4 °C. Before elution, beads were washed three times with RIPA buffer containing 100 nM TRAM 1. Proteins were then eluted off the beads by boiling in 60 µl of elution buffer (5% SDS, 20 mM dithiothreitol (DTT)) at 95 °C for 10 min. Half the volume of the eluate and 2 µg of protein input and flowthrough were loaded onto a 4–12% Bis-Tris gel and separated by SDS-PAGE. The gel was then transferred onto a nitrocellulose membrane and blocked with 5% milk in TBS-T for 1 h at room temperature. The membrane was incubated with primary antibody overnight at 4 °C, and washed three times with TBS-T. Subsequently, the membrane was incubated with secondary antibody for 1 h at room temperature and washed three times with TBS-T for visualization with an Odyssey CLx Imager (LI-COR).

For pulldown of METAP2, 50 µg of protein extract was diluted to a total volume of 200 µl in RIPA buffer and incubated with 50 µl of magnetic agarose beads (Chromotek, GFP Trap (GTMA-20)). TRAM 11 was added to a final concentration of 100 nM and the solution was rotated overnight at 4 °C. Before elution, beads were washed three times with RIPA buffer. Proteins were then eluted off the beads by boiling in 60 µl of elution buffer (5% SDS, 20 mM DTT) at 95 °C for 10 min. Half the volume of the eluate and 2 µg of protein were loaded for the input and flow-through lanes onto 4–12% Bis-Tris gel and separated by SDS-PAGE. The gel was then transferred onto a nitrocellulose membrane and blocked with 5% milk in TBS-T for 1 h at room temperature. The membrane was incubated with primary antibody overnight at 4 °C, and washed three times with TBS-T. Subsequently, the membrane was incubated with secondary antibody for 1 h at room temperature and washed three times with TBS-T for visualization with an Odyssey CLx Imager (LI-COR).

## Immunoprecipitations for immunoblotting of endogenous tagged proteins

For immunoprecipitation of endogenous SOS1, 4 mg of protein extract was diluted to a total volume of 250 µl in RIPA buffer and incubated with 50 µl of magnetic agarose beads (Chromotek, GFP Trap (GTMA-20)), overnight at 4 °C. Before elution, beads were washed three times with RIPA buffer. Proteins were then eluted off the beads by boiling in 60 µl of elution buffer (5% SDS, 20 mM DTT) at 95 °C for 10 min. Half the volume of the eluate and 50 µg of protein were loaded for the input, flowthrough and wild-type HEK293T cell lanes onto 4–12% Bis-Tris gel and separated by SDS-PAGE. The gel was then transferred onto a nitrocellulose membrane and blocked with 5% milk in TBS-T for 1 h at room temperature. The membrane was incubated with primary antibody overnight at 4 °C, and washed three times with TBS-T. Subsequently, the membrane was incubated with secondary antibody for 1 h at room temperature and washed three times with TBS-T for visualization with an Odyssey CLx Imager (LI-COR).

## Sodium arsenite treatment and imaging

Adherent cells were plated (25,000 cells per well in an eight-well chamber slide) 2 d before the experiment. At 1 d before treatment, cells were treated with doxycycline to a final working concentration of  $1 \mu\text{g ml}^{-1}$  in 250 µl of complete growth medium. On the day of the experiment, cells were treated with 30 µM sodium arsenite in 250 µl of complete phenol red-free medium for an hour to induce stress granule formation. After an hour, small-molecule solutions were added directly into

the medium in the well, and cells were incubated for another 3 h. Cells were then washed three times with PBS and fixed with 4% paraformaldehyde in PBS for 15 min at room temperature, washed three times and permeabilized with 0.1% Triton for 5 min on ice. Cells were blocked in 10% goat serum in PBS for 1 h at room temperature then incubated with primary antibody overnight at 4 °C. Cells were washed with PBS three times, then incubated with secondary antibody and DAPI for 1 h at room temperature. Cells were washed with PBS and imaged with a Nikon A1R confocal microscope using a Plan Fluor ×60 oil immersion, 1.30-NA objective. The microscope was equipped with a 405 nm violet laser, a 488 nm blue laser, a 561 nm green laser and a 639 nm laser. Images were exported and analysed using the FIJI software package.

For continuous imaging, adherent cells were plated (25,000 cells per ml) in a 24-well glass-bottom plate (CELLTREAT, Scientific Products, catalogue no. 229125) 2 d before treatment. At 1 d before treatment, cells were treated with doxycycline to a final working concentration of 1 µg ml<sup>-1</sup> in 500 µl of complete growth medium.

On the day of imaging, medium in the well was replaced with complete phenol red-free medium containing 2 µg ml<sup>-1</sup> Hoechst 33342 and 10 µM sodium arsenite. After an hour, the medium in the wells was replaced with complete phenol red-free medium containing 2 µg ml<sup>-1</sup> Hoechst 33342, 10 µM sodium arsenite and the requisite concentration of small molecule. Immediately after treatment was administered, timelapse imaging was initiated. The plate was maintained at 37 °C with 5% CO<sub>2</sub> in a stage top incubator (Okolab) over the course of 2.5 h. Images were acquired by manually capturing images every 5 min at a fixed field of view. The Nikon A1R confocal microscope Plan Fluor ×60 oil immersion, 1.30-NA objective was used.

#### DRG neuron collection and culturing

All animals were housed and experiments performed in accordance with the US National Institutes of Health guidelines for the care and use of laboratory animals, and were approved by Stanford University's Administrative Panel on Laboratory Animal Care (APLAC no. 20608). At 2 d before collection of primary DRG cells, 250 µl of poly-D lysine (PDL) was added to the bottom of an eight-well chamber slide to coat the bottom of the wells evenly. The slide was incubated at 37 °C in a sterile environment. The next day, PDL was removed and the wells were washed with tissue culture-grade sterile water. The chamber slide was left to dry with the lid open within a sterile biosafety cabinet for about 1 h. The slides were subsequently wrapped with parafilm then left in a 4 °C refrigerator.

**Explant collection.** Primary DRG cells were isolated from embryonic (day 17.5–18.5) Sprague-Dawley rats (Charles River Laboratories). A timed pregnant rat was euthanized with carbon dioxide and the embryos retrieved and kept in ice-cold HBSS (Corning, catalogue no. 21-023-CM) supplemented with 10 mM HEPES (Gibco, catalogue no. 15630130). The embryo was decapitated, the ventral organs were removed and the body oriented with the dorsal side facing up. Under a dissection microscope, the skin and the spinal cord were removed and individual DRGs were extracted from either side of the cavity between spinal levels. DRGs from the same embryo were placed in the same 1.5 ml tube. The DRGs were kept in HBSS-HEPES on ice until dissection of all embryos was complete (2–3 h). The DRGs were then placed on a Petri dish on ice and any extra membranes around the DRGs were removed under the dissection microscope. These DRGs were then aseptically transferred into a laminar flow hood and washed with 10 × 1 ml of sterile HBSS-HEPES. After the final wash, the DRGs were resuspended in complete medium, which consists of neurobasal (Gibco, catalogue no. 12348017) medium supplemented with 1% GlutaMAX (Gibco, catalogue no. 35050061), 2% B-27 (Gibco, catalogue no. 17504044), 1% penicillin/streptomycin, 2.5 mg ml<sup>-1</sup> D-glucose (Sigma, catalogue no. G7021) and 50 ng ml<sup>-1</sup> NGF (2.5S beta subunit from Cedarlane Laboratories,

catalogue no. CLMCNET-001.25) that was pre-equilibrated in a humidified 5% CO<sub>2</sub> incubator at 37 °C for 30 min. Single DRGs were seeded in the middle of a PDL-coated well in 20 µl of medium. The chamber slide was left to incubate at 37 °C for 30 min in a 5% CO<sub>2</sub> incubator to allow DRGs to adhere, then 250 µl of neurobasal medium supplemented with 40 µM 5-fluoro-2'-deoxyuridine (FUDR; Sigma, catalogue no. F0503) and 50 ng ml<sup>-1</sup> NGF was carefully added to the well. Neurobasal medium supplemented with FUDR and NGF was replaced every other day.

#### AAV production

On day 0, HEK293T cells were seeded in a six-well plate for 70% confluence on day 1. On day 1, HEK293T cells were co-transfected with plasmids encoding the transgene, RepCap2 and adenoviruses E4, E2A and VA using the PEIMAX transfection reagent according to the manufacturer's protocol. The morning of day 2, medium was replaced with complete DMEM. On day 3, the viral supernatant was removed and filtered through a 0.45 µm filter.

#### DRG neuron infection with AAV

Two days after explant seeding, medium in the wells was replaced with 250 µl of 0.2-µm-filtered neurobasal medium supplemented with FUDR (40 mM) and NGF (50 ng ml<sup>-1</sup>). Then, 8 µl of NMMAT1 transgene viral supernatant and 12 µl of EcDHFR transgene viral supernatant were added to each well. Next, 4 d after infection, neurons were examined for transgene expression.

#### Axotomy and neuron imaging

Before axotomy, fluorescence images of entire explants were acquired in an epi-fluorescence microscope (Leica DMI 6000B) using a ×10 (0.32-NA) objective. The microscope was equipped with an ORCA-Flash4.0 Digital CMOS camera, a Lumencor SOLA light source and filter sets: 370-39/409/448-63 nm (blue emission), 484-25/505/524-32 nm (green emission), 560-32/581/607-40 nm (red emission) and 640-19/655/680-30 nm (far-red emission).

A biopsy punch (1.0 mm, Royaltek) was sterilized with 70% EtOH, then dipped into neurobasal medium. The biopsy punch was used to sever the cell body from the neurites. The detached cell body was then extracted with sterilized tweezers. To ensure complete removal of the cell body, fluorescence images of entire explants were acquired again in an epi-fluorescence microscope (Leica DMI 6000B) using a ×10 (0.32-NA) objective after axotomy.

To observe degeneration of the neurites, axon termini and the proximal axon region were imaged with a Nikon A1R confocal microscope using a Plan Fluor ×60 oil immersion objective at 0 h, 3 h, 6 h, 12 h, 24 h, 48 h, 72 h and 96 h after injury. Sample size choice was made to be at least  $n > 3$  for a given condition. No randomization of samples or blinding was performed.

#### Axonal degeneration quantification

Axon degeneration was quantified using a degeneration index calculated using ImageJ (v.1.53) as previously described<sup>57</sup>. In brief, mRuby3 signal was used as a marker of the axon. The mRuby3 channel images were binarized, such that axons were converted to white and all other regions black. The total number of white pixels was defined as total axon area. Axonal fragmentation in degenerating axons leads to their particulate structure, unlike healthy axons which are continuous and intact. To detect degenerated axons, we used the particle analyser module of ImageJ and counted the area of particles. As we used a ×60 objective, particles were defined as having a size of 0–30,000 pixels and circularity above 0.2 (ref. 58). The degeneration index was calculated as the ratio of fragmented axon area over total axon area.

#### Synthetic chemistry

All synthetic chemistry procedures are available in the Supplementary Information.

# Article

## DNA sequences

All DNA sequences used can be found in the Supplementary Information.

## Reporting summary

Further information on research design is available in the Nature Portfolio Reporting Summary linked to this article.

## Data availability

All data supporting the findings of this study are available within the Article, Extended Data Figs. 1–15, Supplementary Information or associated data tables. All single-cell quantification data are available upon request.

## Code availability

All new code generated for the data analysis pipeline is available at <https://github.com/cngsc/RAFL>.

56. Sakuma, T., Nakade, S., Sakane, Y., Suzuki, K.-I. T. & Yamamoto, T. MMEJ-assisted gene knock-in using TALENs and CRISPR–Cas9 with the PITCh systems. *Nat. Protoc.* **11**, 118–133 (2016).

57. Sasaki, Y., Vohra, B. P. S., Lund, F. E. & Milbrandt, J. Nicotinamide mononucleotide adenylyl transferase-mediated axonal protection requires enzymatic activity but not increased levels of neuronal nicotinamide adenine dinucleotide. *J. Neurosci.* **29**, 5525–5535 (2009).
58. Gerdts, J., Sasaki, Y., Vohra, B., Marasa, J. & Milbrandt, J. Image-based screening identifies novel roles for IκB kinase and glycogen synthase kinase 3 in axonal degeneration. *J. Biol. Chem.* **286**, 28011–28018 (2011).

**Acknowledgements** We thank M. Gray for experimental assistance. This work was supported by an A\*STAR fellowship to C.S.C.N. This work was supported in part by grant no. DP2GM154016 from the NIH/NIGMS.

**Author contributions** C.S.C.N. and S.M.B. conceived of the project. C.S.C.N. conducted all experiments and analysed all data. A.L. and B.C. provided essential expertise in neuron collection and biology. C.S.C.N and S.M.B. wrote the manuscript. S.M.B. provided supervision.

**Competing interests** S.M.B. is a member of the scientific advisory board for Lycia Therapeutics. Stanford University has filed a provisional patent application covering aspects of this work listing S.M.B. and C.S.C.N. as authors. The remaining authors declare no competing interests.

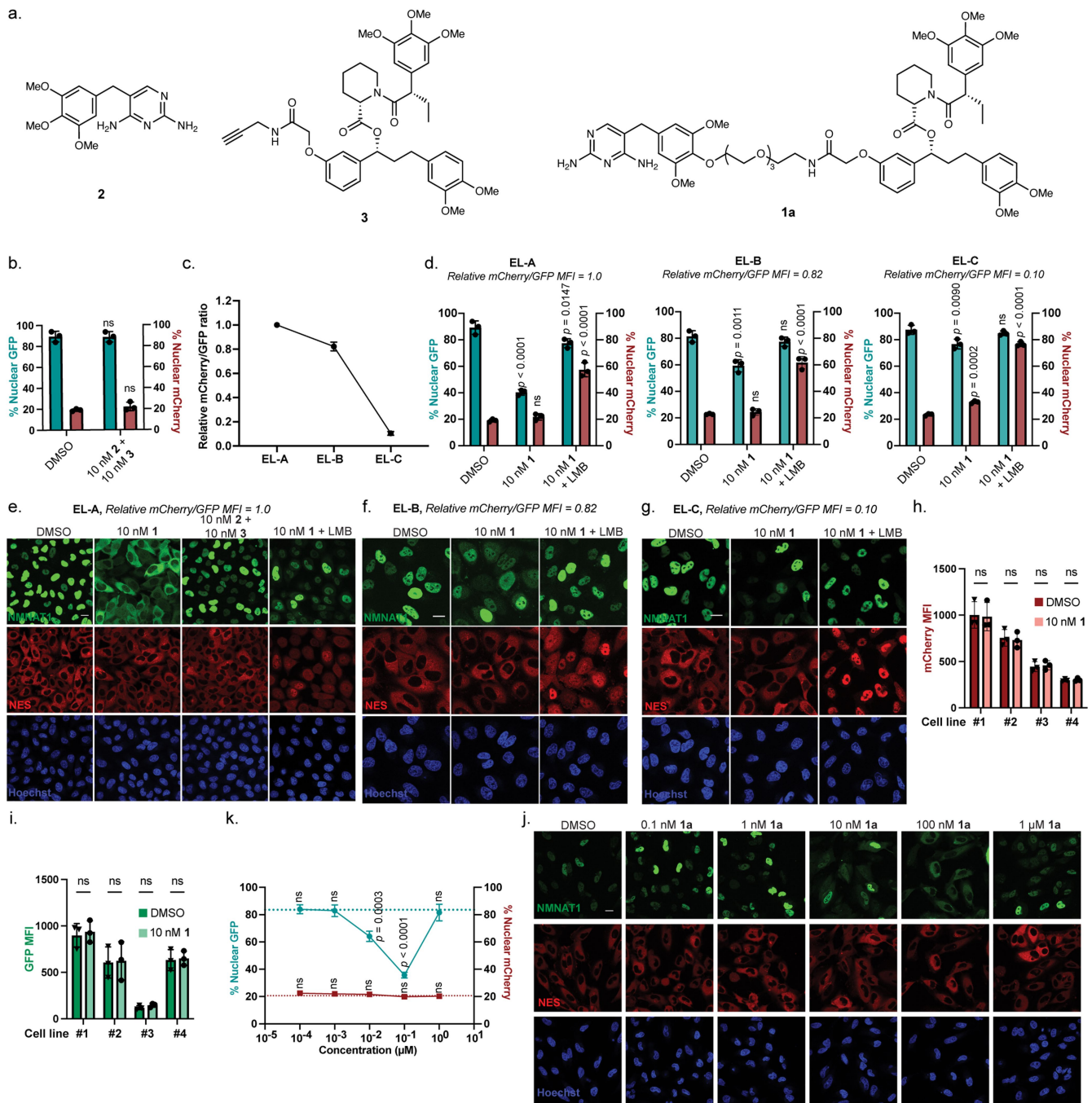
## Additional information

**Supplementary information** The online version contains supplementary material available at <https://doi.org/10.1038/s41586-024-07950-8>.

**Correspondence and requests for materials** should be addressed to Steven M. Banik.

**Peer review information** *Nature* thanks Yue Xiong and the other, anonymous, reviewer(s) for their contribution to the peer review of this work.

**Reprints and permissions information** is available at <http://www.nature.com/reprints>.

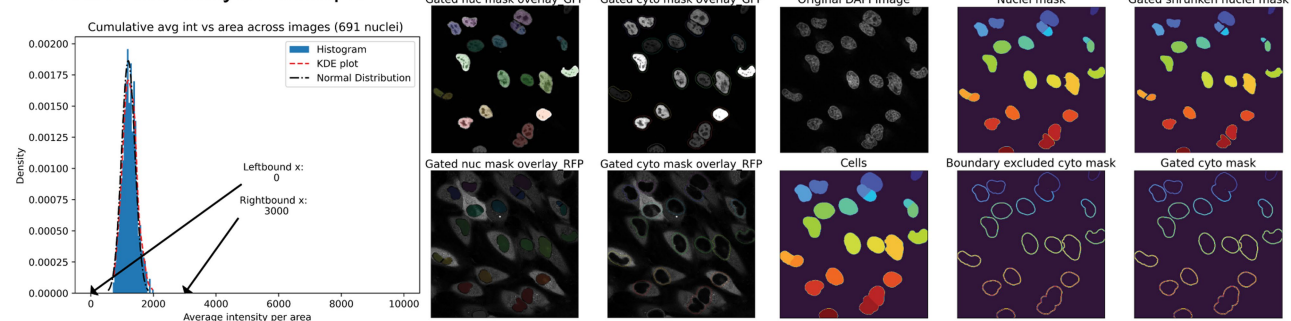


**Extended Data Fig. 1 | Examination of NMNAT1 export cell lines.** **a**, Unlinked warhead controls for **1**: **2**: trimethoprim (TMP), binds *EcDHFR*; **3**: binds FKBP12<sup>F36V</sup>. **1a**, TRAM which engages *EcDHFR* and FKBP12<sup>F36V</sup> containing a (PEG)<sub>3</sub> linker between the warheads. **b**, Localization of either protein upon treatment of **EL-A** with unlinked warheads **2** and **3**. **c**, Comparison of the relative mCherry/GFP median fluorescence intensity ratio between the three isolated clonal export lines (**EL-A-C**). **d**, Ability of three NMNAT1 export lines exhibiting different relative export shuttle (mCherry) to NMNAT1 (GFP) ratios to translocate NMNAT1 from the nucleus promoted by **1** or inhibited by leptomycin B (LMB) after 3-hour treatment. **e**, Representative live-cell images for NMNAT1 relocalization treated with **1** or control molecules, or **1** and leptomycin-B (LMB) in Export Line A (**EL-A**) after 3 h. **f**, Representative live-cell images for NMNAT1 relocalization treated with **1** or **1** and leptomycin-B (LMB) in Export Line B (**EL-B**) after 3 h. **g**, Representative live-cell images for NMNAT1 relocalization treated with **1**, or **1** and leptomycin-B (LMB) in Export Line C (**EL-C**) after 3 h. Levels of

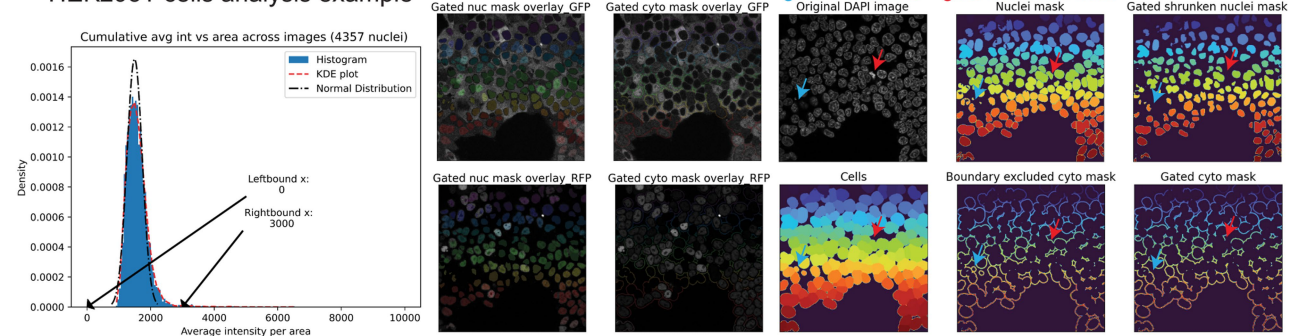
mCherry **h**, and GFP **i**, after treatment with **1** for 3 h across four isolated export cell lines with varying nuclear and cytoplasmic protein expression levels. **j**, Representative live-cell images for NMNAT1 relocalization with export line **EL-A** treated with varying concentrations of **1a**. **k**, Dose response curve of NMNAT1 and NES localization for **EL-A** in response to treatment with **1a**. MFI: Median fluorescence intensity. Images in **e,f,g,j** are representative of three biological replicates. Data in **b,c,d,h,i,k** are mean  $\pm$  s.d. of three independent experiments. Scale bars are 20  $\mu$ m. P values in **b** were determined by unpaired two-tailed t-tests comparing treatment to the DMSO control. NMNAT1 = FKBP12<sup>F36V</sup>-GFP-NMNAT1, NES = mCherry-ecDHFR-NES(HIV-REV1) P values in **d,k** were determined by one-way ANOVA with Dunnett's post hoc test comparing each condition to the DMSO control. P values in **h,i** were determined by two-way ANOVA with Šidák post hoc test comparing the treated condition to the DMSO control for each line. Hoechst stains the nucleus.

# Article

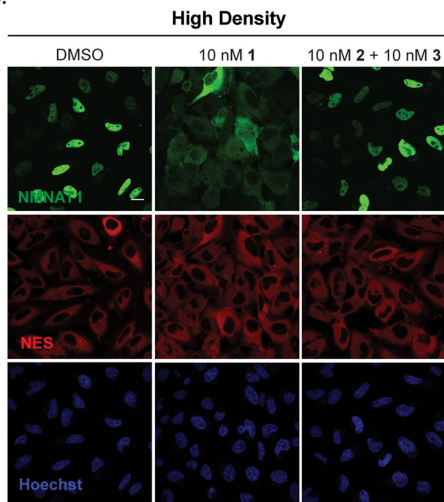
## a. HeLa cells analysis example



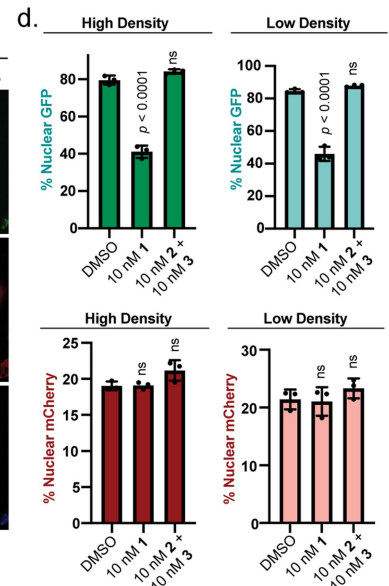
## b. HEK293T cells analysis example



C.

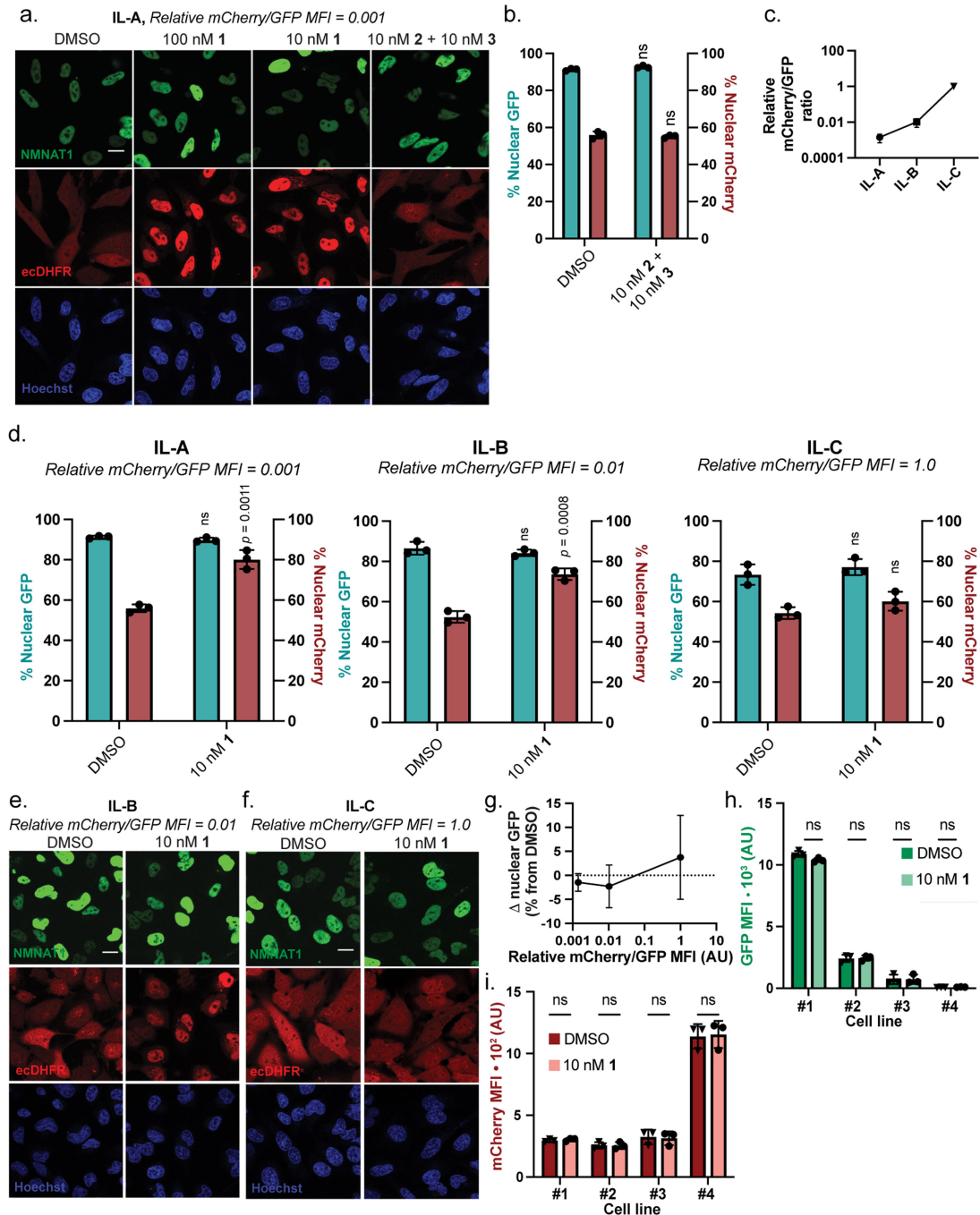


NMNAT1  
NES  
Hoechst



**Extended Data Fig. 2 | Illustration of gating and segmentation pictures automatically generated from analysis pipeline applied to three different cell types.** **a.** Imaging analysis pipeline applied on HeLa cells. Gating histograms generated with the set bounds indicated. Masks for nuclear and cytoplasm areas overlaid onto respective fluorophore images. Cytoplasm areas are circumferentially grown from nuclei masks retaining the relative size between the masks. **b.** Imaging analysis pipeline applied to HEK293T cells. Masks for nuclear and cytoplasm areas overlaid onto respective fluorophore images, with segmentation of highly confluent cells and gating out of dead cells (high

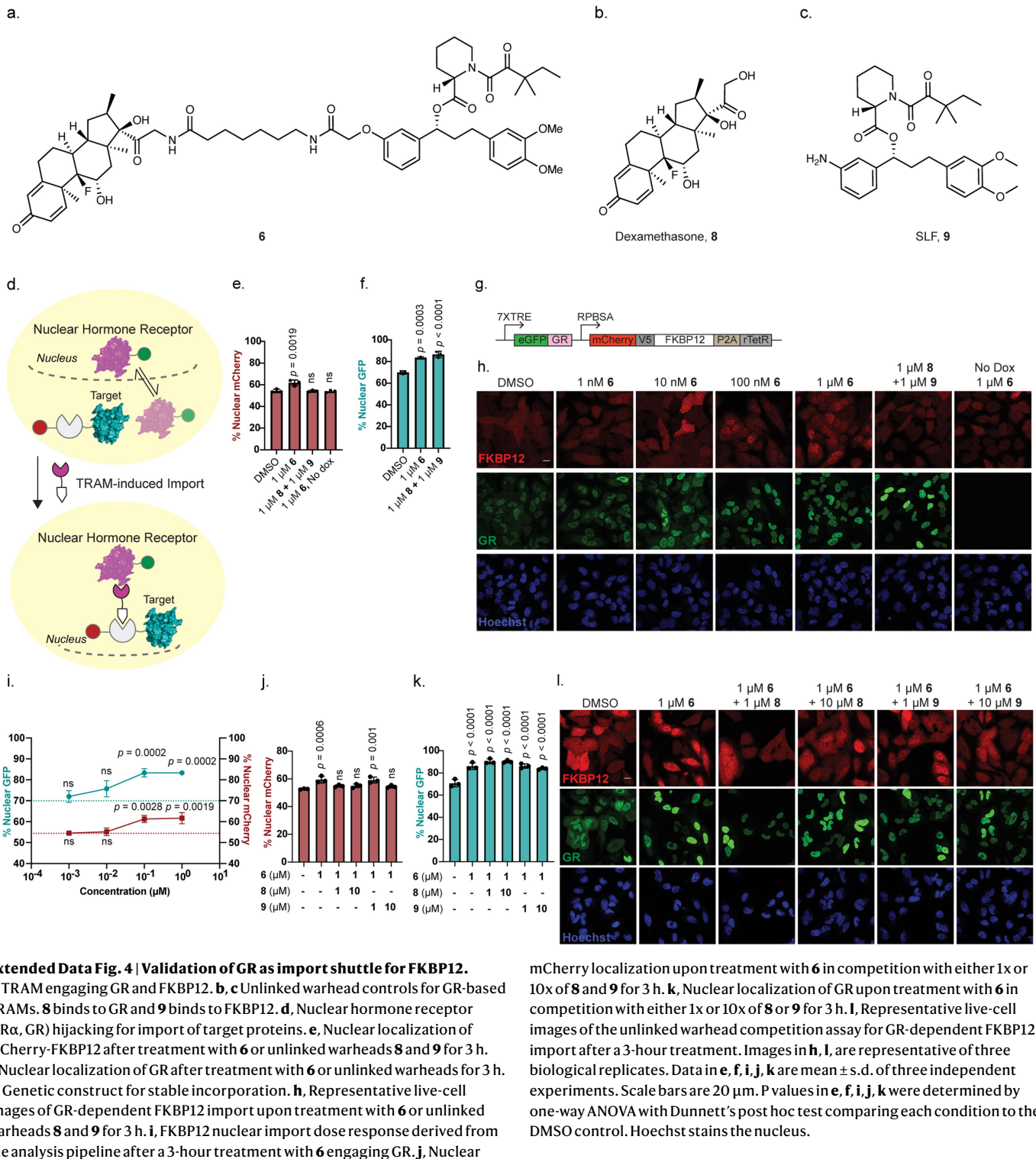
nuclear stain over a small area) and debris. **c.** Representative live-cell images for NMNAT1 relocalization in EL-A treated with 1 or control molecules in cells seeded at high ( $0.04 \times 10^6$  cells) and low density ( $0.01 \times 10^6$  cells). **d.** Quantification of nuclear GFP and mCherry from **c**. Images in **c** are representative of three biological replicates. Data in **d** are mean  $\pm$  s.d. of three independent experiments. Scale bars are 20  $\mu$ m. P values in **d** were determined by one-way ANOVA with Dunnett's post hoc test comparing each condition to the DMSO control. Hoechst stains the nucleus.



**Extended Data Fig. 3 | NMNAT1 can be utilized as a nuclear import shuttle.** **a**, Representative live-cell images of clonal import line A (**IL-A**) upon treatment with **1** or small molecule controls for 3 h. **b**, Quantification of localization upon treatment of the IL-A with unlinked warheads **2** and **3**. **c**, Comparison of the relative mCherry/GFP median fluorescence intensity ratio between the three isolated clonal import lines (**IL-A-C**). **d**, Ability of three representative import cell lines (IL) with different relative target (mCherry) and shuttle (NMNAT1) ratios to redistribute a diffuse protein target after 3-hour treatment with **1**. **e**, Representative live-cell images of clonal import line B (**IL-B**) upon treatment with **1** for 3 h. **f**, Representative live-cell images of clonal import line C (**IL-C**) upon treatment with **1** for 3 h. **g**, Quantification of NMNAT1 protein localization.

change upon treatment with 10 nM **1** in **IL-A-C** possessing different mCherry/GFP ratios. **h**, Levels of GFP after treatment with **1** for 3 h in four isolated import cell lines with varying nuclear protein expression levels. **i**, Levels of mCherry after treatment with **1** for 3 h across four isolated import cell lines with varying diffuse protein expression levels. Images in **a, e, f**, are representative of three biological replicates. Data in **b, c, d, g, h, i** are mean  $\pm$  s.d. of three independent experiments. Scale bars are 20  $\mu$ m. MFI = median fluorescence intensity. P values in **h, i** were determined by two-way ANOVA with Šidák post hoc test comparing the treated condition to the DMSO control for each line. P values in **b, d** were determined by unpaired two-tailed t-tests comparing treatment to the DMSO control.

# Article

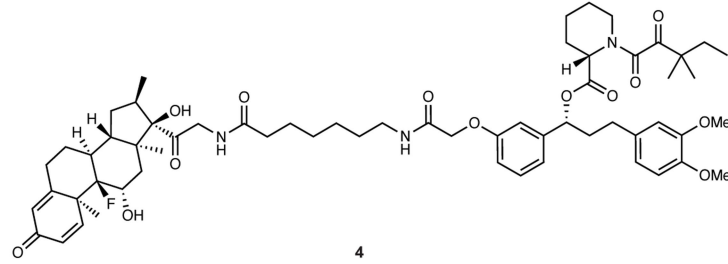


**Extended Data Fig. 4 | Validation of GR as import shuttle for FKBP12.**

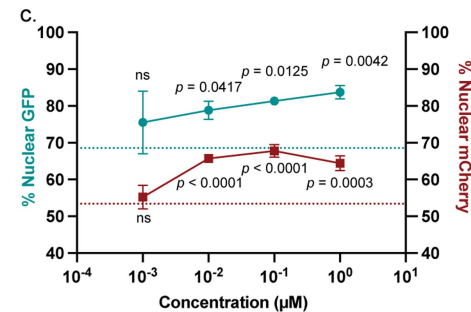
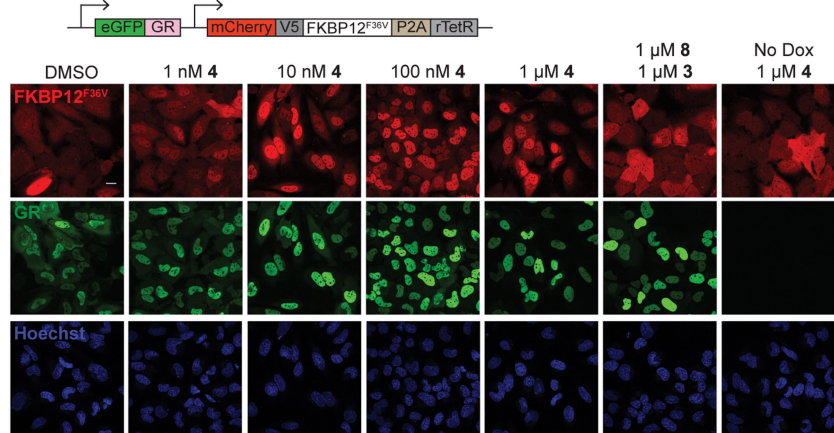
**a.**, TRAM engaging GR and FKBP12. **b, c**, Unlinked warhead controls for GR-based TRAMs. **8** binds to GR and **9** binds to FKBP12. **d**, Nuclear hormone receptor (ER $\alpha$ , GR) hijacking for import of target proteins. **e**, Nuclear localization of mCherry-FKBP12 after treatment with **6** or unlinked warheads **8** and **9** for 3 h. **f**, Nuclear localization of GR after treatment with **6** or unlinked warheads for 3 h. **g**, Genetic construct for stable incorporation. **h**, Representative live-cell images of GR-dependent FKBP12 import upon treatment with **6** or unlinked warheads **8** and **9** for 3 h. **i**, FKBP12 nuclear import dose response derived from the analysis pipeline after a 3-hour treatment with **6** engaging GR. **j**, Nuclear

mCherry localization upon treatment with **6** in competition with either 1x or 10x of **8** and **9** for 3 h. **k**, Nuclear localization of GR upon treatment with **6** in competition with either 1x or 10x of **8** or **9** for 3 h. **l**, Representative live-cell images of the unlinked warhead competition assay for GR-dependent FKBP12 import after a 3-hour treatment. Images in **h**, **l**, are representative of three biological replicates. Data in **e**, **f**, **i**, **j**, **k** are mean  $\pm$  s.d. of three independent experiments. Scale bars are 20  $\mu$ m. P values in **e**, **f**, **i**, **j**, **k** were determined by one-way ANOVA with Dunnett's post hoc test comparing each condition to the DMSO control. Hoechst stains the nucleus.

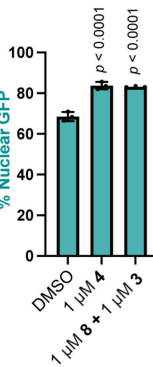
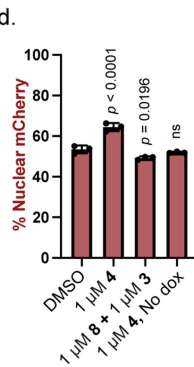
a.



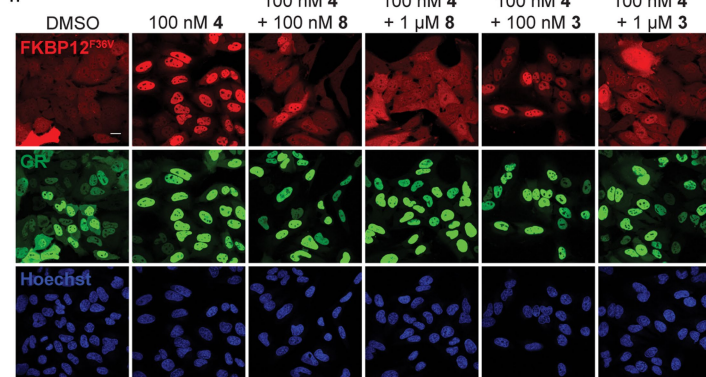
b.



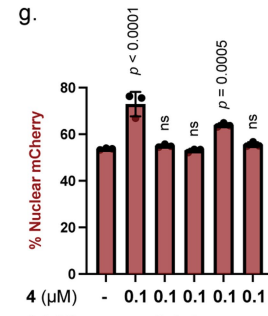
d.



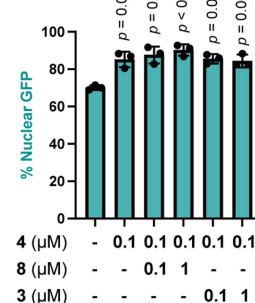
f.



g.



h.

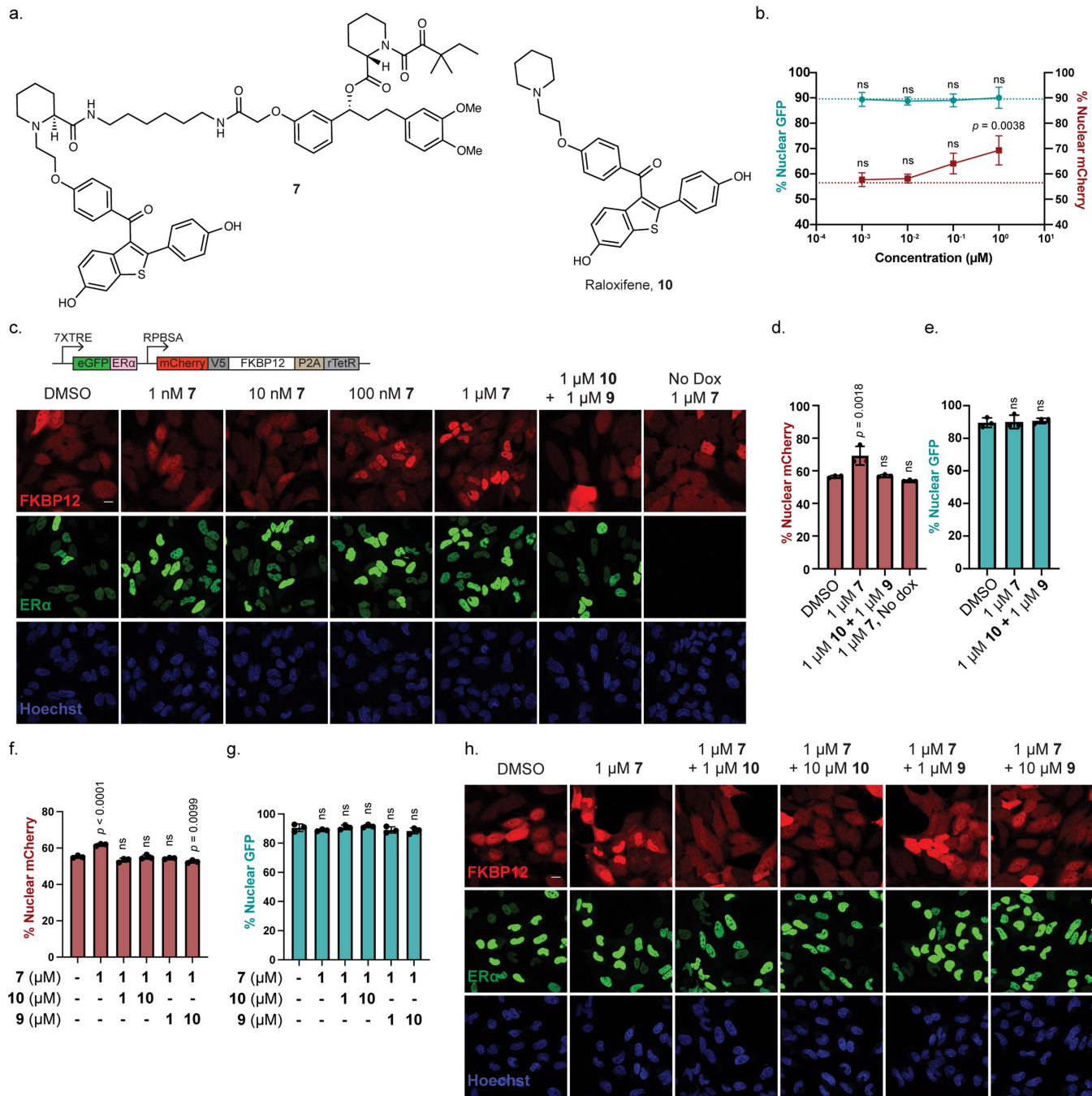


#### Extended Data Fig. 5 | Validation of GR as import shuttle for FKBP12<sup>F36V</sup>.

**a.** TRAM engaging GR and FKBP12<sup>F36V</sup>. **b.** Representative live-cell images of GR dependent FKBP12<sup>F36V</sup> import upon treatment with **4** or unlinked warheads **8** and **3** for 3 h. **c.** FKBP12<sup>F36V</sup> nuclear import dose response derived from the analysis pipeline after a 3-hour treatment with **4** engaging GR. **d.** Nuclear localization of mCherry-FKBP12<sup>F36V</sup> after treatment with **4** or unlinked warheads **3** and **8** for 3 h. **e.** Nuclear localization of GR after treatment with **4** or unlinked warheads **3** and **8** for 3 h. **f.** Representative live-cell images of the

unlinked warhead competition assay for GR-dependent FKBP12<sup>F36V</sup> import after 3-hour treatment. **g.** mCherry localization upon treatment with **4** in competition with either 1x or 10x of **8** or **3** for 3 h. **h.** Nuclear localization of GR upon treatment with **4** in competition with either 1x or 10x of **8** or **3** for 3 h. Images in **b, f,** are representative of three biological replicates. Data in **c, d, e, g, h** are mean ± s.d. of three independent experiments. Scale bars are 20 μm. P values in **c, d, e, g, h** were determined by one-way ANOVA with Dunnett's post hoc test comparing each condition to the DMSO control. Hoechst stains the nucleus.

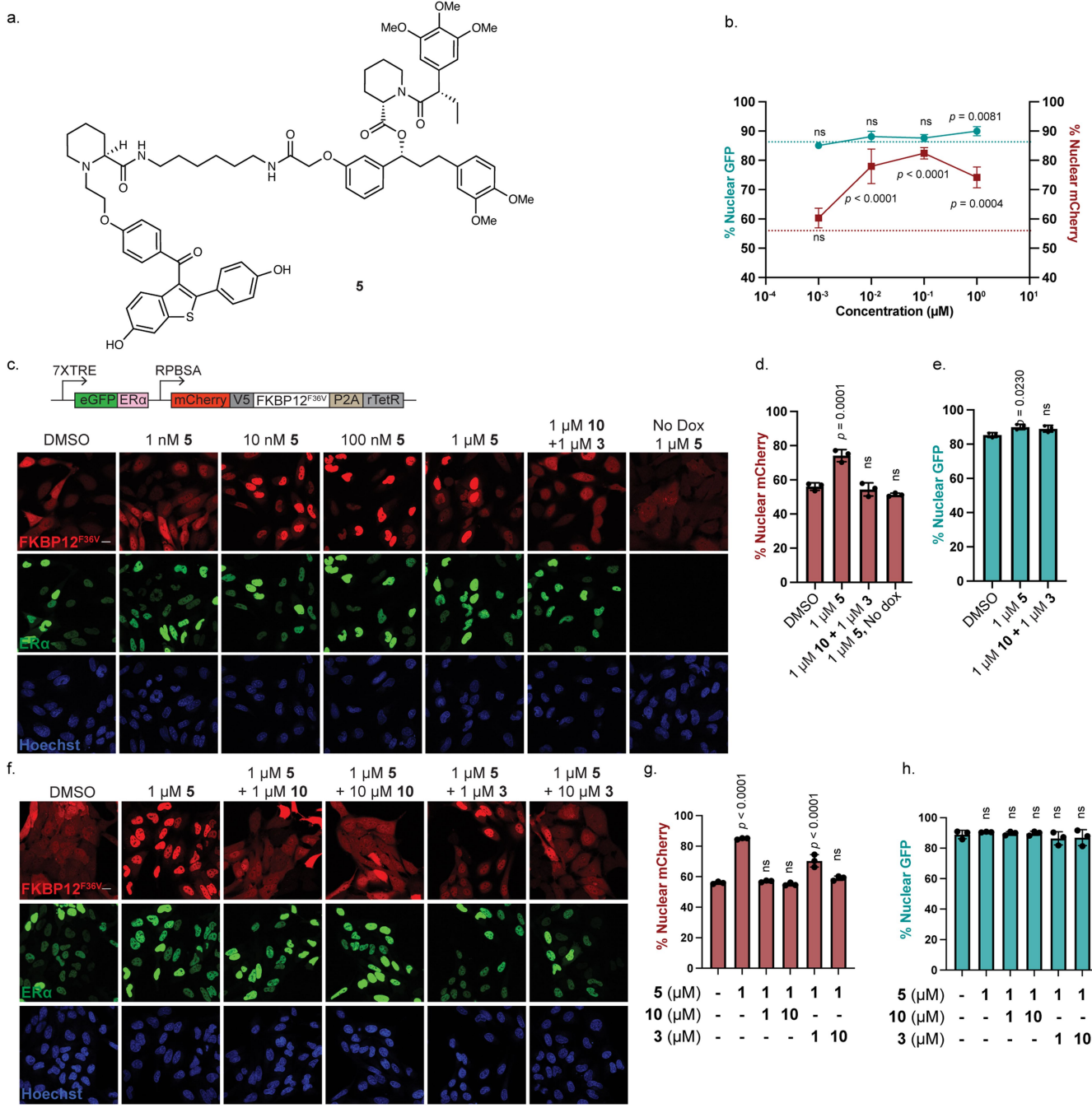
# Article



**Extended Data Fig. 6 | Validation of ER $\alpha$  as import shuttle for FKBP12.**

**a.** TRAM engaging ER $\alpha$  and FKBP12, raloxifene (**10**) unlinked control binds to ER $\alpha$ . **b.** FKBP12 nuclear import dose response derived from the analysis pipeline after a 3-hour treatment with **7** engaging ER $\alpha$ . **c.** Representative live-cell images of ER $\alpha$ -dependent FKBP12 import upon treatment with **7** or unlinked warheads **10** and **9** for 3 h. **d.** Nuclear localization of mCherry-FKBP12 after treatment with **7** or unlinked warheads **10** and **9** for 3 h. **e.** Nuclear localization of ER $\alpha$  after treatment with TRAM **7** or unlinked warheads **10** and **9** for 3 h. **f.** Nuclear mCherry localization upon treatment with **7** in competition with either 1x or 10x of **10** or **9** for 3 h. **g.** Nuclear localization of ER $\alpha$  upon treatment with **7** in competition with either 1x or 10x of **10** or **9** for 3 h. **h.** Representative live-cell images of the unlinked warhead competition assay for ER $\alpha$ -dependent FKBP12 import after a 3-hour treatment. Images in **c-h** are representative of three biological replicates. Data in **b-d**, **e**, **f**, **g** are mean  $\pm$  s.d. of three independent experiments. Scale bars are 20  $\mu\text{m}$ . P values in **b-d**, **e**, **f**, **g**, were determined by one-way ANOVA with Dunnett's post hoc test comparing each condition to the DMSO control. Hoechst stains the nucleus.

**9** for 3 h. **g**, Nuclear localization of ER $\alpha$  upon treatment with **7** in competition with either 1x or 10x of **10** or **9** for 3 h. **h**, Representative live-cell images of the unlinked warhead competition assay for ER $\alpha$ -dependent FKBP12 import after a 3-hour treatment. Images in **c-h** are representative of three biological replicates. Data in **b-d**, **e**, **f**, **g** are mean  $\pm$  s.d. of three independent experiments. Scale bars are 20  $\mu\text{m}$ . P values in **b-d**, **e**, **f**, **g**, were determined by one-way ANOVA with Dunnett's post hoc test comparing each condition to the DMSO control. Hoechst stains the nucleus.

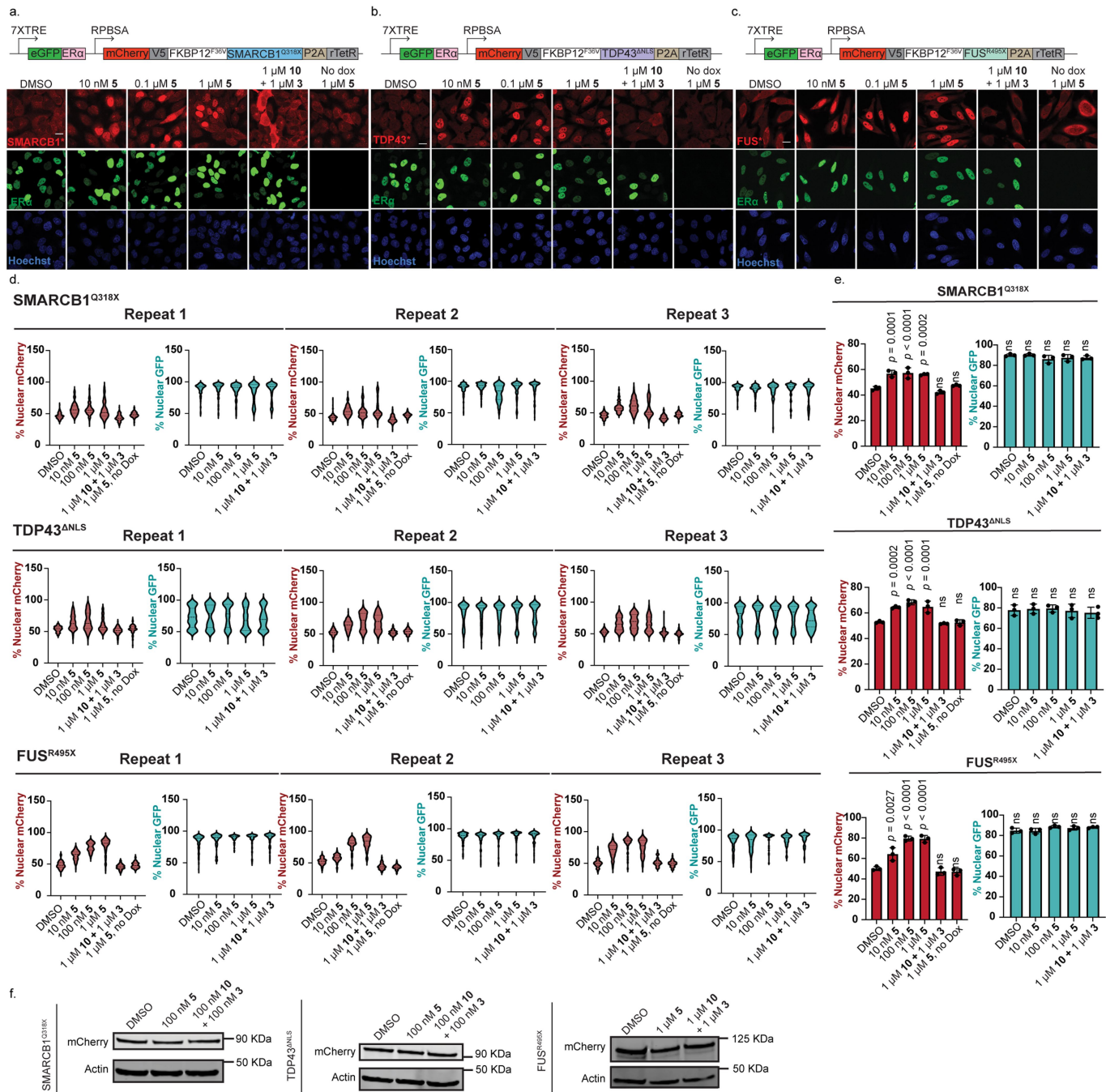


**Extended Data Fig. 7 | Validation of ERα as import shuttle for FKBP12<sup>F36V</sup>.**

**a.** TRAM engaging ERα and FKBP12<sup>F36V</sup>. **b.** FKBP12<sup>F36V</sup> nuclear import dose response derived from the analysis pipeline after a 3-hour treatment with **5** engaging ERα. **c.** Representative live-cell images of ERα-dependent FKBP12<sup>F36V</sup> import upon treatment with **5** or unlinked warheads **3** and **10** for 3 h. **d.** Nuclear localization of mCherry-FKBP12<sup>F36V</sup> after treatment with **5** or unlinked warheads **3** and **10** for 3 h. **e.** Nuclear localization of ERα after treatment with **5** or unlinked warheads **3** and **10** for 3 h. **f.** Representative live-cell images of the

unlinked warhead competition assay for ERα-dependent FKBP12<sup>F36V</sup> import for 3 h. **g.** mCherry localization upon treatment with **5** in competition with either 1x or 10x of **3** or **10** for 3 h. **h.** Nuclear localization of ERα upon treatment with **5** in competition with either 1x or 10x of **3** or **10** for 3 h. Images in **c, f, g** are representative of three biological replicates. Data in **b, d, e, g, h** are mean ± s.d. of three independent experiments. Scale bars are 20 μm. P values in **b, d, e, g, h** were determined by one-way ANOVA with Dunnett's post hoc test comparing each condition to the DMSO control. Hoechst stains the nucleus.

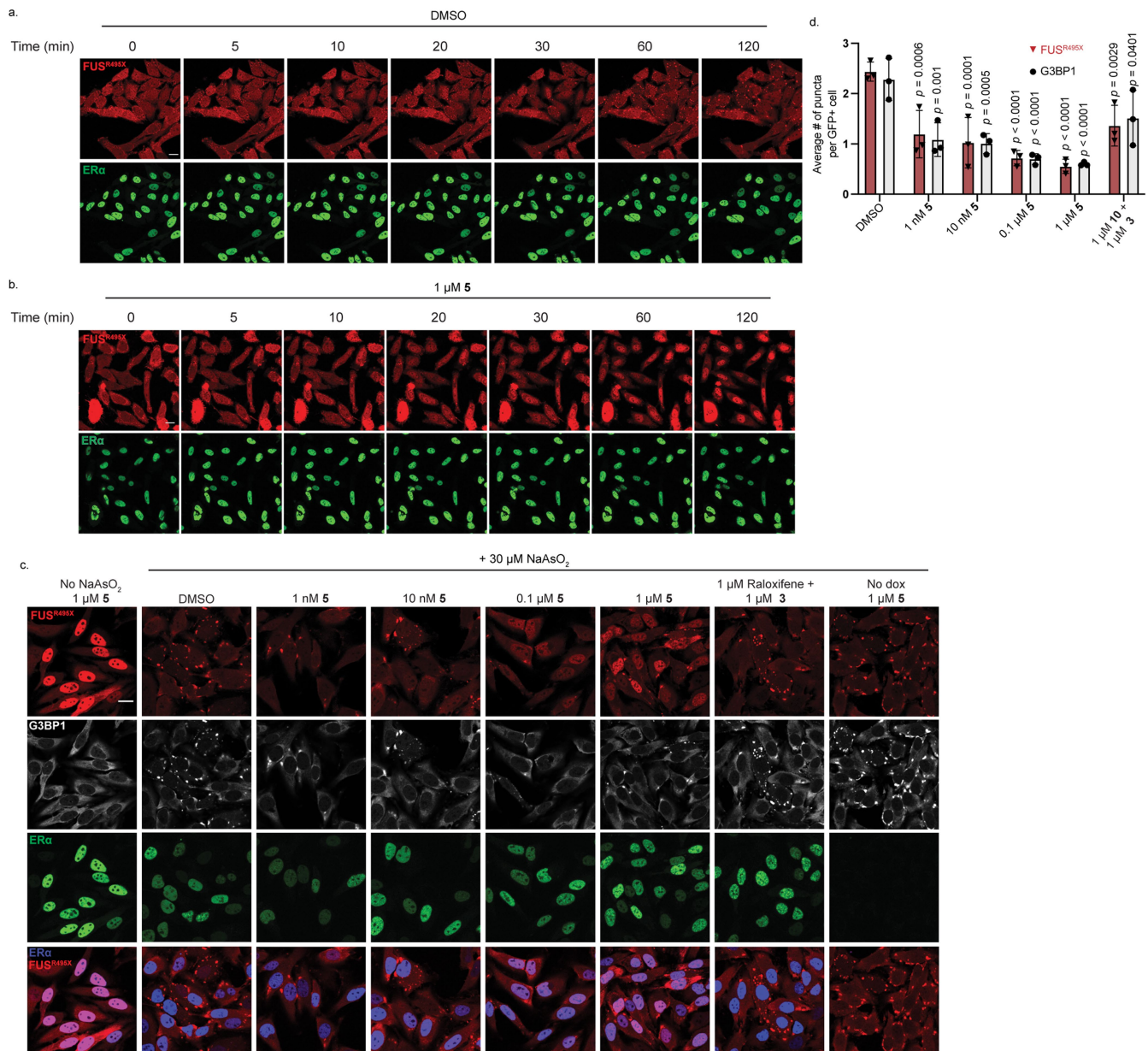
# Article



**Extended Data Fig. 8 | Nuclear import of mutant proteins with ERα.**

**a.** Representative live-cell images of HeLa cells stably expressing target mutant protein SMARCB1<sup>Q318X</sup> (SMARCB1\*) and ERα under an inducible promoter after a 3-hour treatment of **5**. **b.** Representative live-cell images of HeLa cells stably expressing target mutant protein TDP43<sup>ΔNLS</sup> (TDP\* = TDP43<sup>K82A/R83A/K84A</sup>) and ERα under an inducible promoter after a 3-hour treatment of **5**. **c.** Representative live-cell images of HeLa cells stably expressing target mutant protein FUS<sup>R495X</sup> (FUS\*) and ERα under an inducible promoter after a 3-hour treatment of **5**. **d.** Violin plots of the distribution of respective target mutant protein and ERα in the three cell lines under different treatment conditions, across 3 repeats.

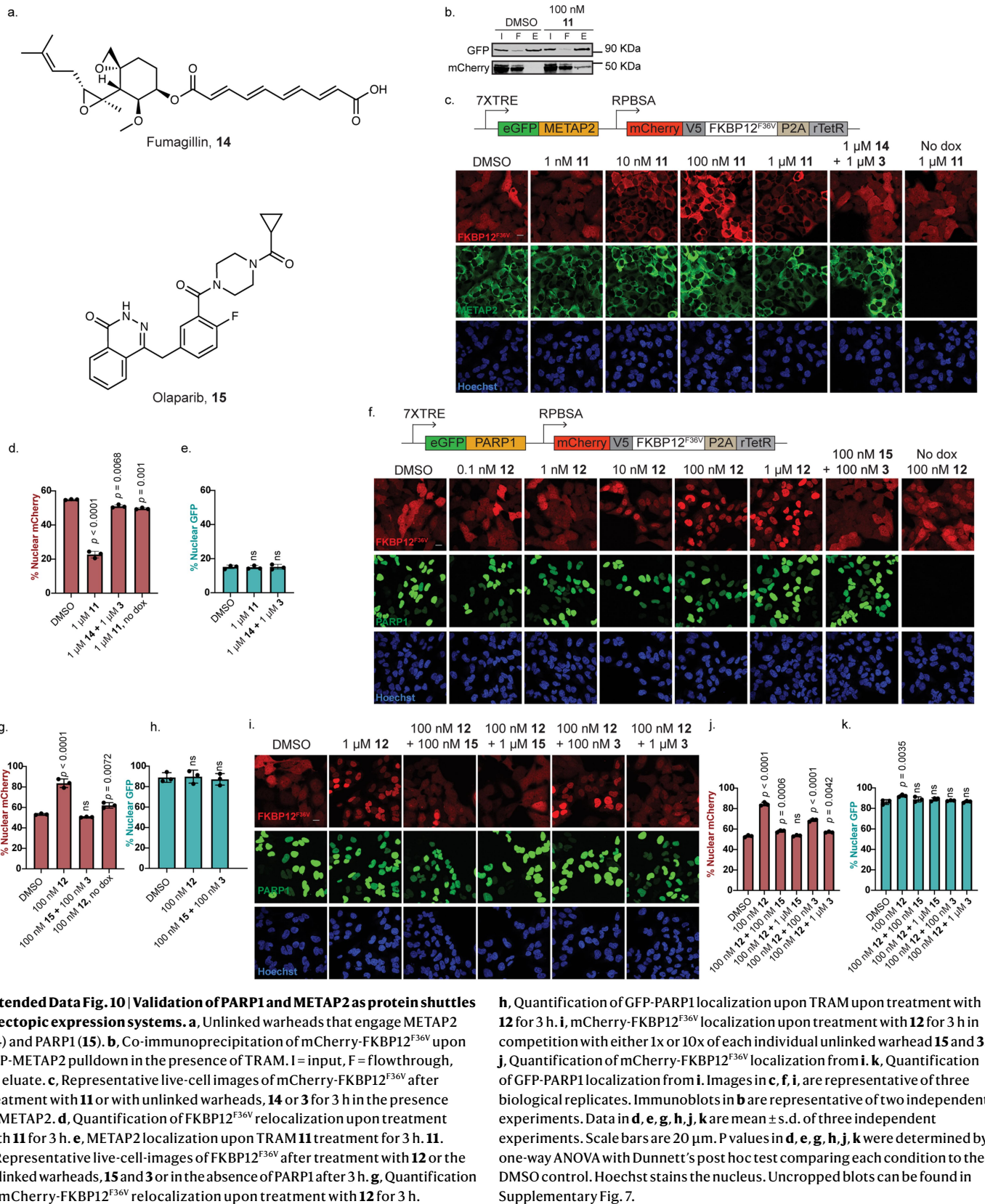
**e.** Mean percent nuclear target protein and ERα upon treatment with **5** for 3 h in HeLa cells stably expressing the target mutant protein and ERα under an inducible promoter. **f.** Representative immunoblot of mutant proteins after a 3-hour treatment with **5**. Images in **a, b, c** are representative of three biological replicates. Data in **e**, is mean  $\pm$  s.d. of three independent experiments. Data in **f** is representative of two independent experiments. P values in **e** were determined by one-way ANOVA comparing each condition to the DMSO control. Scale bars are 20  $\mu$ m. Hoechst stains the nucleus. Uncropped blots can be found in Supplementary Fig. 7.

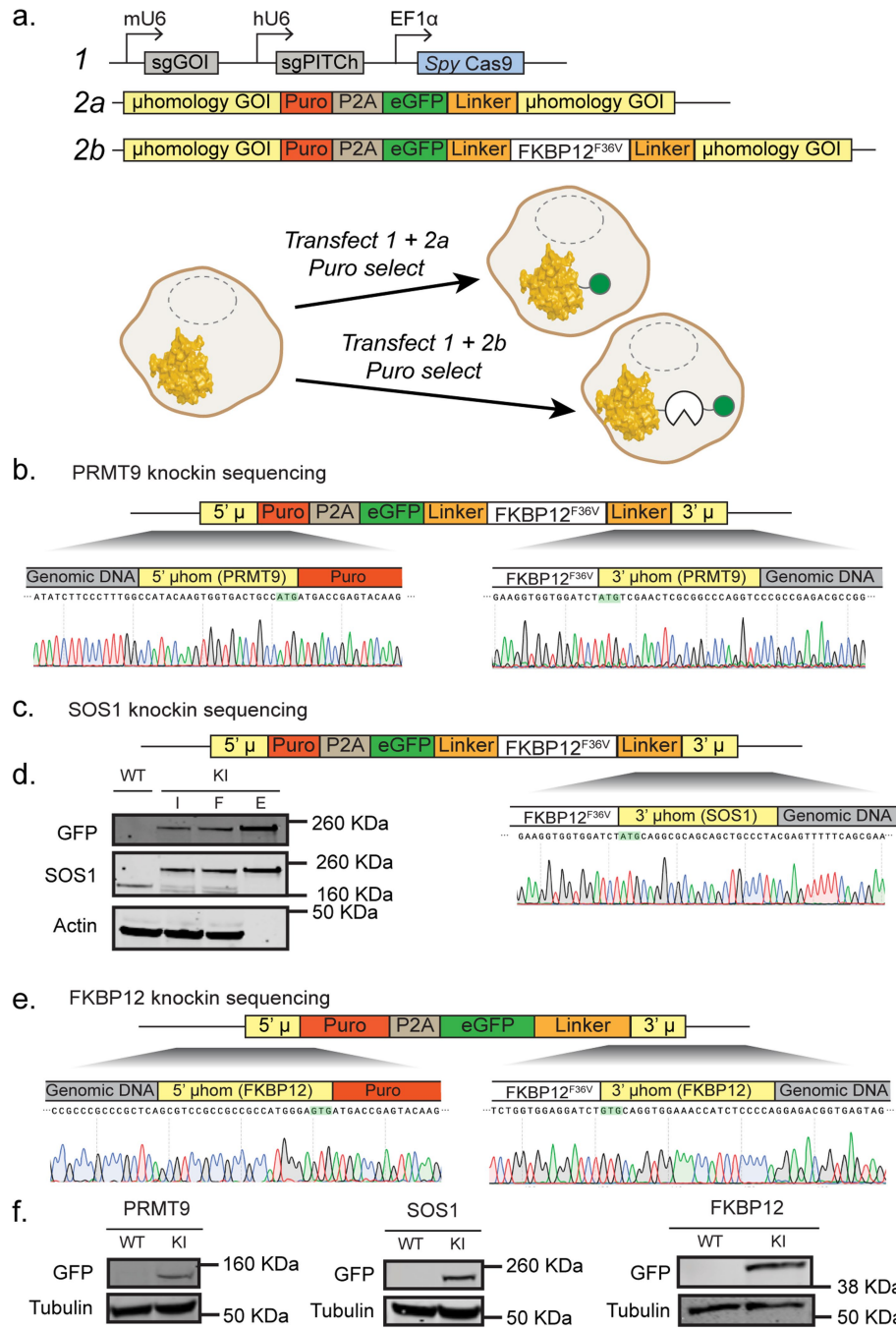


**Extended Data Fig. 9 | TRAM-mediated protein relocalization from stress granules.** **a**, Timelapse imaging snapshots of FUS<sup>R495X</sup> when cells are treated with DMSO after stress granule formation. **b**, Timelapse imaging snapshots of FUS<sup>R495X</sup> extraction from granules when cells are treated with **5**. **c**, Representative fixed-cell immunofluorescent images of stress granule marker G3BP1 and mCherry-FUS<sup>R495X</sup> after treatment with **5** or control compounds for 3 h. **d**, Quantification of stress granules in cells after treatment with varying

concentrations of **5** or control compounds for 3 h. Images in **c** are representative of three biological replicates. Images in **a**, **b** are representative of two independent experiments. Data in **d** are mean  $\pm$  s.d. of three independent experiments. Scale bars are 20  $\mu$ m. P values in **d** were determined by two-way ANOVA with Dunnett's post hoc test comparing each condition to their DMSO control.

# Article

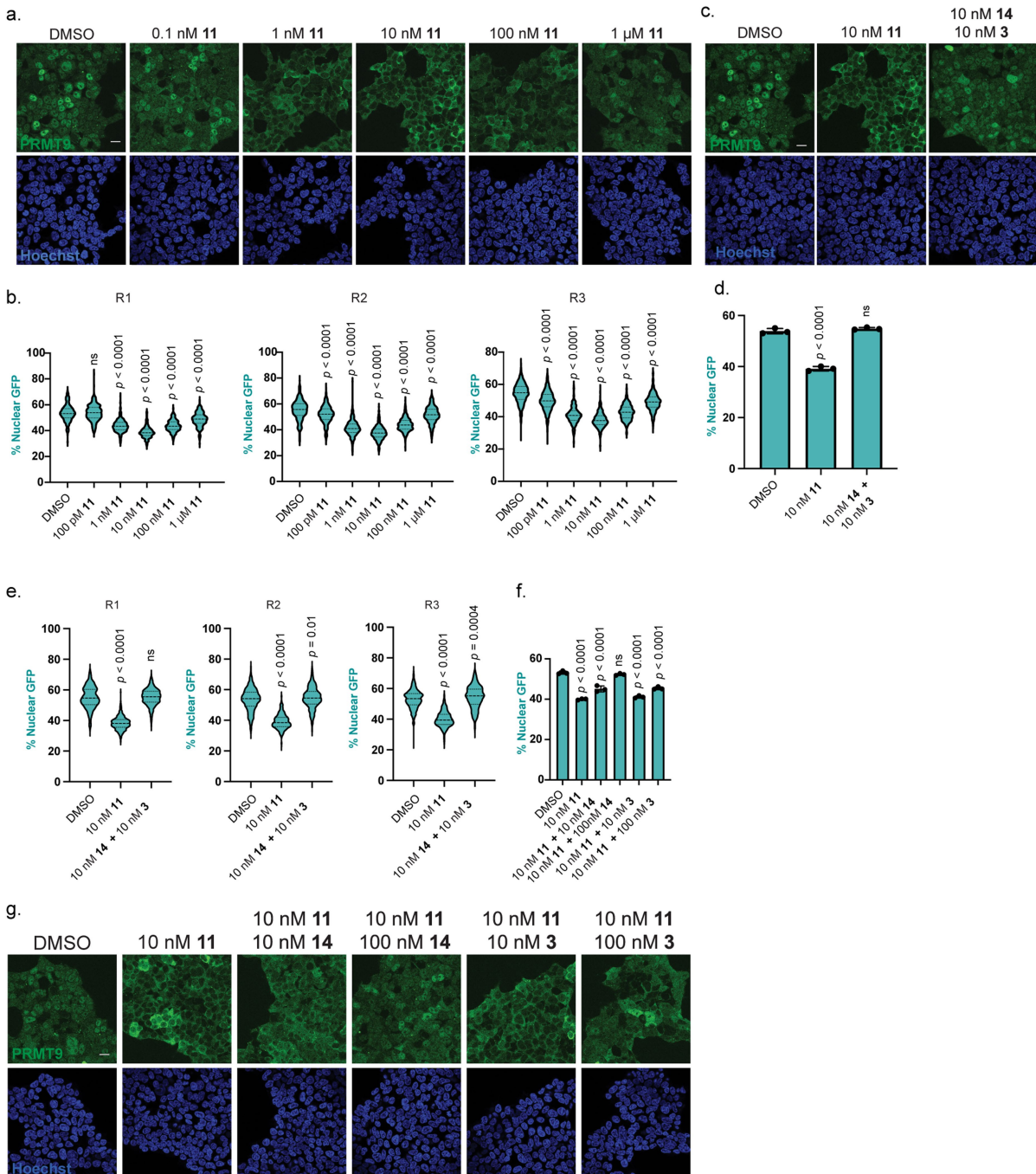




**Extended Data Fig. 11 | Validation of Cas9-CRISPR mediated endogenously tagged lines.** **a.** Schematic for modified PITCh knock-in into target proteins. **b.** Sequencing of the regions near the N terminus of the endogenous PRMT9 gene after donor cassette insertion into endogenous PRMT9. **c.** Sequencing of the region downstream the N terminus of the endogenous SOS1 gene after donor cassette insertion into endogenous SOS1. **d.** Due to high GC content of the genomic region upstream of the N terminus of SOS1, immunoblotting was

used to validate successful incorporation of donor cassette onto endogenous SOS1 after GFP pulldown, I = input, F = flowthrough, E = eluate. **e.** Sequencing of the regions near the N terminus of the endogenous FKBP12 gene after donor cassette insertion into endogenous FKBP12. **f.** Demonstration of GFP-FKBP12<sup>F36V</sup> tagging of endogenous PRMT9, SOS1 and GFP tagging of endogenous FKBP12 in HEK293T cells. Immunoblots in **d,f** are representative of two independent experiments. Uncropped blots can be found in Supplementary Fig. 7.

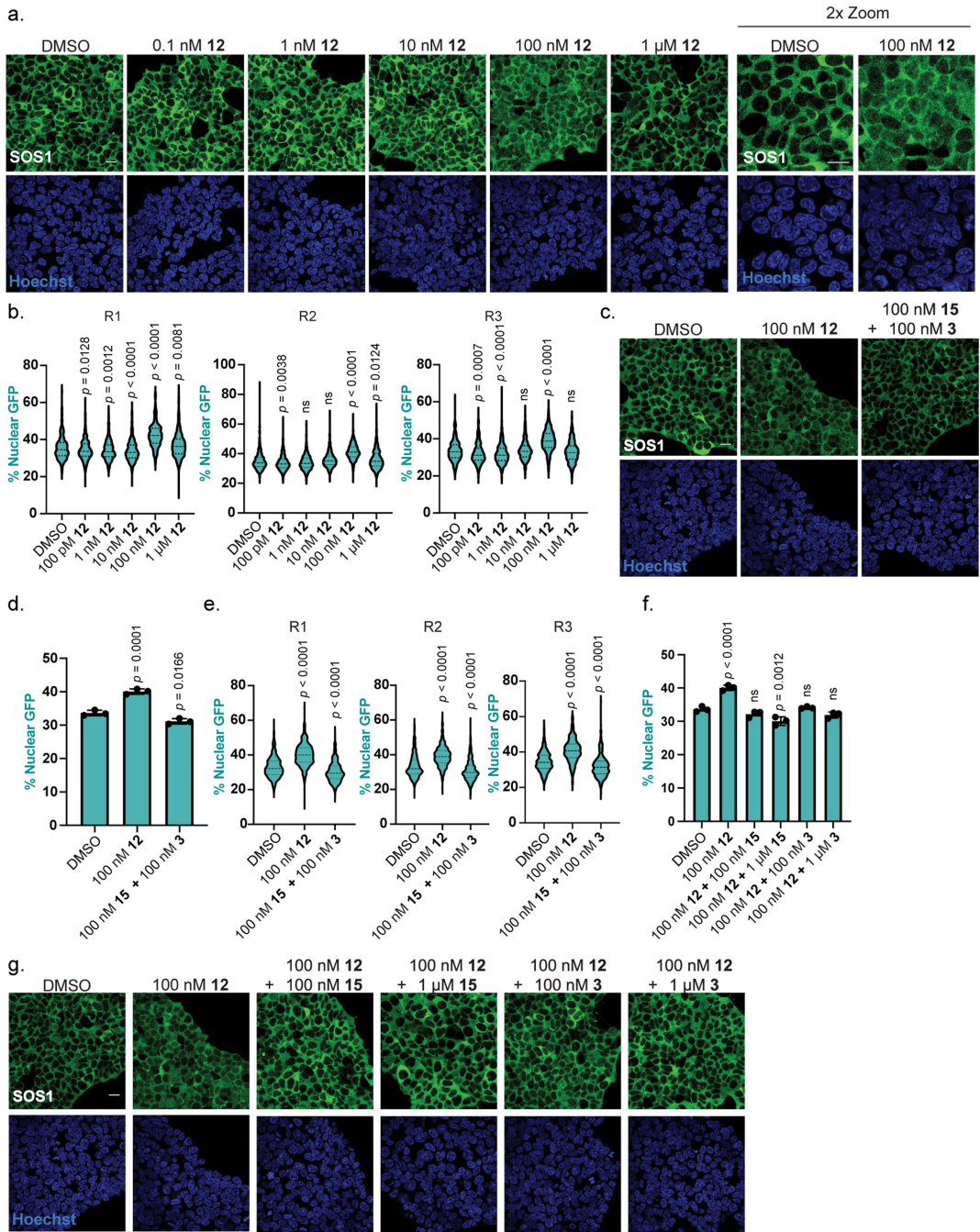
# Article



**Extended Data Fig. 12 | METAP2 as an endogenous nuclear export shuttle to relocalize endogenous PRMT9.** **a.**, Representative live-cell images of endogenous PRMT9 localization upon treatment with different concentrations of TRAM **11** for 24 h. **b.**, Violin plots illustrating the homogenous population shift in PRMT9 localization upon TRAM **11** treatment at different concentrations for 24 h. **c.**, Representative live-cell images of endogenous PRMT9 localization upon treatment with unlinked warheads **14** and **3** for 24 h. **d.**, Quantification of localization changes observed in **c**. **e.**, Violin plots showcasing the lack of homogenous population shift in PRMT9 localization when treated with the

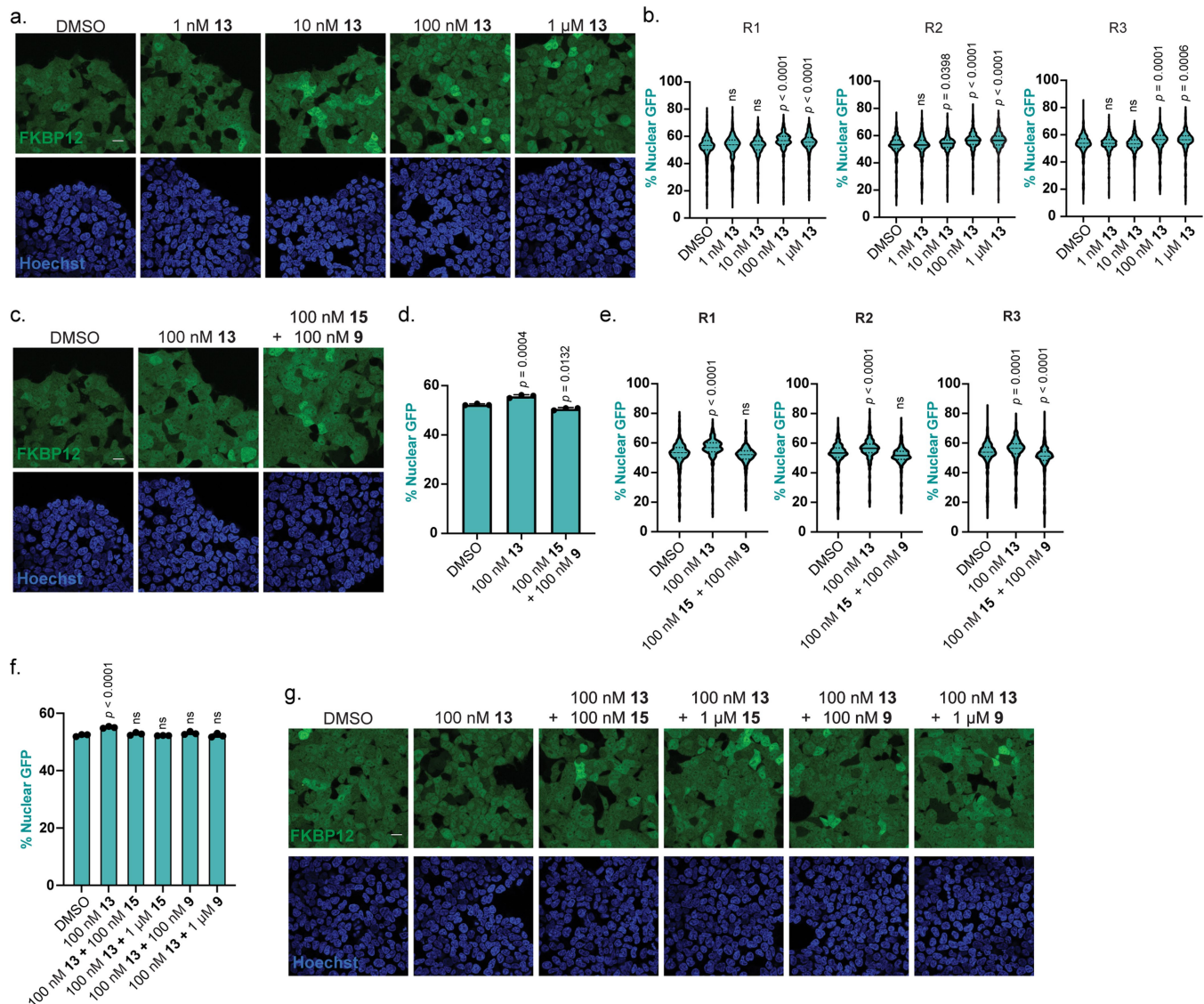
unlinked warheads **14** and **3** versus TRAM **11** for 24 h. **f.**, Quantification of the change in PRMT9 localization upon treatment with **11** after pre-treatment for 1 h with either 1x or 10x of **14** or competed with 1x, or 10x of **3** for 24 h.

**g.**, Representative images of the competition assay quantified in **f**. Images in **a**, **c**, **g** are representative of three biological replicates. Data in **d**, **f**, **g** are mean  $\pm$  s.d. of three independent experiments. Scale bars are 20  $\mu$ m. P values in **b**, **d**, **e**, **f** were determined by one-way ANOVA with Dunnett's post hoc test comparing each condition to the DMSO control. Hoechst stains the nucleus.



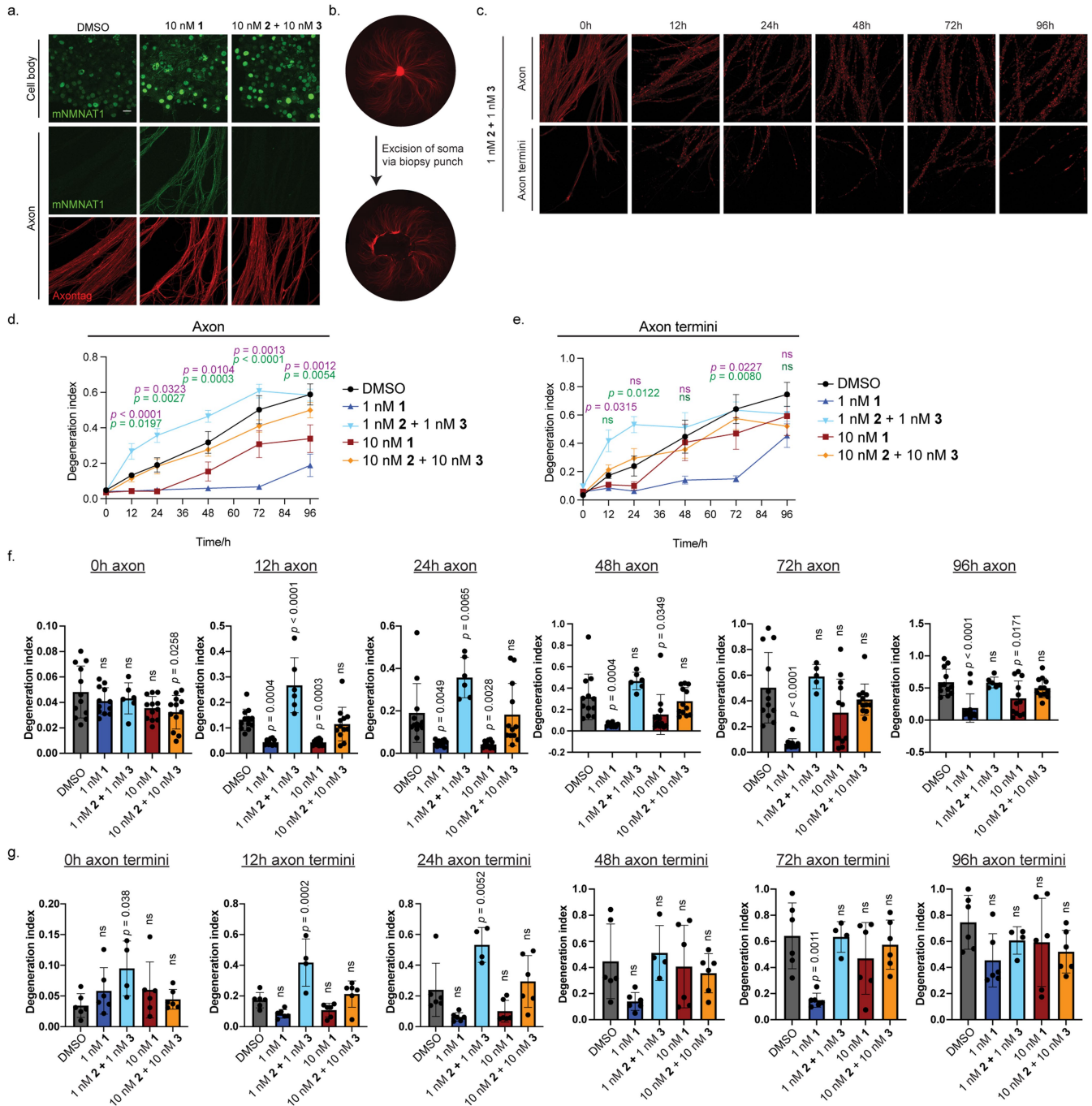
**Extended Data Fig. 13 | PARP1 as an endogenous nuclear import shuttle to relocate endogenous SOS1. a,** Representative live-cell images of endogenous SOS1 localization upon treatment with different concentrations of TRAM 12 for 24 h. **b,** Violin plots illustrating the homogenous population shift in SOS1 localization upon TRAM 12 treatment at different concentrations for 24 h. **c,** Representative live-cell images of endogenous SOS1 localization after treatment with unlinked warheads 15 and 3 for 24 h. **d,** Quantification of localization changes observed in c. **e,** Violin plots showcasing the lack of homogenous population shift in SOS1 localization when treated with the

unlinked warheads 15 and 3 versus TRAM 12 for 24 h. **f,** Quantitation of change in SOS1 localization upon treatment with 12 in competition with either 1x or 10x of 15 or 3 for 24 h. **g,** Representative images of SOS1 localization in the competition assay in f. Images in a, c, g are representative of three biological replicates. Data in d, f are mean  $\pm$  s.d. of three independent experiments. Scale bars are 20  $\mu$ m. P values in b, d, e, f were determined by one-way ANOVA with Dunnett's post hoc test comparing each condition to the DMSO control. Hoechst stains the nucleus.



**Extended Data Fig. 14 | PARP1 as an endogenous nuclear import shuttle to relocalize endogenous FKBP12. a.** Representative live-cell images of partial endogenous FKBP12 localization upon treatment with different concentrations of TRAM 13 for 24 h. **b.** Violin plots illustrating a homogenous population shift in FKBP12 localization upon TRAM 13 treatment at different concentrations for 24 h. **c.** Representative live-cell images of endogenous FKBP12 localization after treatment with unlinked warheads 15 and 9 for 24 h. **d.** Quantification of localization changes observed in c. **e.** Violin plots showcasing the lack of homogenous population shift in FKBP12 localization when treated with the

unlinked warheads 15 and 9 versus TRAM 13 for 24 h. **f.** Quantification of the change in FKBP12 localization upon treatment with 13 in competition with either 1x or 10x of 15 or 9 for 24 h. **g.** Representative images of FKBP12 localization in the competition assay in f. Images in a, c, g are representative of three biological replicates. Data in d, f are mean  $\pm$  s.d. of three independent experiments. Scale bars are 20  $\mu$ m. P values in b, d, e, f were determined by one-way ANOVA with Dunnett's post hoc test comparing each condition to the DMSO control. Hoechst stains the nucleus.



#### Extended Data Fig. 15 | Nuclear export of NMNAT1 in neurons.

**a.** Representative live-cell images of NMNAT1 upon treatment with TRAM1 or unlinked warheads 2 and 3 at 10 nM for 24 h. **b.** Representative images of before and after axotomy on explants. Axotomies were performed using a biopsy punch, the mRuby3-Axontag protein serves as an axonal marker, Axontag = GAP43at-mRuby3-ecDHFR. **c.** Representative images of axons and axon termini post-axotomy, that have been pre-treated with unlinked controls for 24 h prior. **d.** Representative images of mNMNAT1 in axons after exposure to 1 for 24 h followed by axotomy. mRuby3 signal was used to monitor degeneration across treated neurons. **d.** Quantification of axon degeneration over time. **e.** Quantification of axon degeneration over time in axon termini. **f.** Comparison of the degeneration index in axona at different time points with different treatment conditions. **g.** Comparison of the degeneration index (DI) in the axon termini at different time points with different treatment conditions. DI was calculated as the ratio of fragmented axon area over total axon area.

For plots in **d, f, g**, a total of 12 replicates derived from 4 different embryos were combined in the plots for all conditions except 1nM 2 + 1nM 3. A total of 6 replicates derived from 2 different embryos were combined in the plots for the 1nM 2 + 1nM 3 condition. For plots in **e, g**, a total of 6 replicates derived from 4 different embryos were combined in the plots for all conditions except 1nM 2 + 1nM 3. A total of 4 replicates derived from 2 different embryos were combined in the plots for the 1nM 2 + 1nM 3 condition. Data in **d, e** is shown as the mean  $\pm$  s.e.m. values. Data in **f, g**, is shown as the mean  $\pm$  s.d. values. P values in **d, e**, were determined by two-way ANOVA with Tukey's post hoc test comparing the 1nM treatment of 1 with the DMSO (purple) or the unlinked warhead control (green) at each time point. P values in **f, g**, were determined by one-way ANOVA with Dunnett's post hoc test comparing each treatment to the DMSO control at each time point. Images in **a, b, c** are representative of neurons harvested from 4 different embryos. Scale bars are 20  $\mu$ m.

## Reporting Summary

Nature Portfolio wishes to improve the reproducibility of the work that we publish. This form provides structure for consistency and transparency in reporting. For further information on Nature Portfolio policies, see our [Editorial Policies](#) and the [Editorial Policy Checklist](#).

### Statistics

For all statistical analyses, confirm that the following items are present in the figure legend, table legend, main text, or Methods section.

n/a Confirmed

- The exact sample size ( $n$ ) for each experimental group/condition, given as a discrete number and unit of measurement
- A statement on whether measurements were taken from distinct samples or whether the same sample was measured repeatedly
- The statistical test(s) used AND whether they are one- or two-sided  
*Only common tests should be described solely by name; describe more complex techniques in the Methods section.*
- A description of all covariates tested
- A description of any assumptions or corrections, such as tests of normality and adjustment for multiple comparisons
- A full description of the statistical parameters including central tendency (e.g. means) or other basic estimates (e.g. regression coefficient) AND variation (e.g. standard deviation) or associated estimates of uncertainty (e.g. confidence intervals)
- For null hypothesis testing, the test statistic (e.g.  $F$ ,  $t$ ,  $r$ ) with confidence intervals, effect sizes, degrees of freedom and  $P$  value noted  
*Give  $P$  values as exact values whenever suitable.*
- For Bayesian analysis, information on the choice of priors and Markov chain Monte Carlo settings
- For hierarchical and complex designs, identification of the appropriate level for tests and full reporting of outcomes
- Estimates of effect sizes (e.g. Cohen's  $d$ , Pearson's  $r$ ), indicating how they were calculated

*Our web collection on [statistics for biologists](#) contains articles on many of the points above.*

### Software and code

Policy information about [availability of computer code](#)

Data collection	BD CSampler Plus or FACS Diva (v 8.0) were used for flow cytometry data acquisition. NIS Elements (v 5.11.00) was used for confocal fluorescence microscopy image acquisition. Image Studio Software (v 5.2) was used for Western blot scanning. Las-X (Leica v 3.7.6.25997) was used for acquiring epifluorescence microscopy images.
Data analysis	Code used to analyse relative fluorescence localisation is available for download at <a href="https://github.com/cngsc/RAFL">https://github.com/cngsc/RAFL</a> . Microsoft Excel (v 16.23) and Graphpad Prism (v 9.0) were used for data analysis. FlowJo (v 10.0) was used for flow cytometry data analysis. FIJI (ImageJ v 1.53) was used for fluorescence microscopy image analysis. Image Studio Software (v 5.2) was used for Western blot quantification.

For manuscripts utilizing custom algorithms or software that are central to the research but not yet described in published literature, software must be made available to editors and reviewers. We strongly encourage code deposition in a community repository (e.g. GitHub). See the Nature Portfolio [guidelines for submitting code & software](#) for further information.

## Data

Policy information about [availability of data](#)

All manuscripts must include a [data availability statement](#). This statement should provide the following information, where applicable:

- Accession codes, unique identifiers, or web links for publicly available datasets
- A description of any restrictions on data availability
- For clinical datasets or third party data, please ensure that the statement adheres to our [policy](#)

All data relevant to the manuscript are included. Further details and information are available from the corresponding author upon request.

## Research involving human participants, their data, or biological material

Policy information about studies with [human participants or human data](#). See also policy information about [sex, gender \(identity/presentation\), and sexual orientation](#) and [race, ethnicity and racism](#).

Reporting on sex and gender

n/a

Reporting on race, ethnicity, or other socially relevant groupings

n/a

Population characteristics

n/a

Recruitment

n/a

Ethics oversight

n/a

Note that full information on the approval of the study protocol must also be provided in the manuscript.

## Field-specific reporting

Please select the one below that is the best fit for your research. If you are not sure, read the appropriate sections before making your selection.

Life sciences

Behavioural & social sciences

Ecological, evolutionary & environmental sciences

For a reference copy of the document with all sections, see [nature.com/documents/nr-reporting-summary-flat.pdf](https://nature.com/documents/nr-reporting-summary-flat.pdf)

## Life sciences study design

All studies must disclose on these points even when the disclosure is negative.

Sample size

All experiments in cell lines were performed independently at least three times in accordance with standard cell and molecular biology procedures. Imaging experiment fields of view were chosen to ensure representative population capture. At least three fields of view were captured per condition for cell line imaging experiments. Neuron experiment sample sizes were consistent with prior reports (Felman et al. Proc. Natl. Acad. Sci. 2022).

Data exclusions

Data in single-cell plots comparing ratio of fluorescent proteins to protein trafficking were excluded if their fluorescence ratios were  $>3$  standard deviations from the mean. These represent statistical outliers reflecting errors in expression of one of the fluorescent proteins.

Replication

All data were successfully replicated with multiple independent biological replicates as indicated in the Figure legends. Neuronal experiments were performed on DRGs obtained from at least two different rat embryos.

Randomization

No formal randomization was performed as internal controls were employed for quantitative comparisons. This study is not a randomized control trial and randomization is not conventionally performed for in cellulo studies.

Blinding

The investigator was not blinded as machine-based measurement of physical and chemical properties are usually unaffected by knowledge of the sample. Technical and analytical requirements preclude blinding, but standardized protocols for analysis mitigate the ability to bias results.

## Reporting for specific materials, systems and methods

We require information from authors about some types of materials, experimental systems and methods used in many studies. Here, indicate whether each material, system or method listed is relevant to your study. If you are not sure if a list item applies to your research, read the appropriate section before selecting a response.

## Materials & experimental systems

n/a	Involved in the study
<input type="checkbox"/>	<input checked="" type="checkbox"/> Antibodies
<input type="checkbox"/>	<input checked="" type="checkbox"/> Eukaryotic cell lines
<input checked="" type="checkbox"/>	<input type="checkbox"/> Palaeontology and archaeology
<input type="checkbox"/>	<input checked="" type="checkbox"/> Animals and other organisms
<input checked="" type="checkbox"/>	<input type="checkbox"/> Clinical data
<input checked="" type="checkbox"/>	<input type="checkbox"/> Dual use research of concern
<input checked="" type="checkbox"/>	<input type="checkbox"/> Plants

## Methods

n/a	Involved in the study
<input checked="" type="checkbox"/>	<input type="checkbox"/> ChIP-seq
<input type="checkbox"/>	<input checked="" type="checkbox"/> Flow cytometry
<input checked="" type="checkbox"/>	<input type="checkbox"/> MRI-based neuroimaging

## Antibodies

### Antibodies used

MC FKBP12 (mouse, Abcam ab58072 [1E5-A12], 1:1000)  
 MC GFP (mouse, Santa Cruz Biotechnology sc-9996, 1: 500)  
 MC β-Actin (rabbit, Cell Signaling Technology mAb #4970, 1: 1000)  
 PC Vinculin (rabbit, Cell Signaling Technology mAb #4650 1: 1000)  
 PC α-Tubulin (rabbit, Cell Signaling Technology mAb #2144 1: 1000)  
 MC G3BP1 (mouse, Santa Cruz Biotechnology sc-365338 1: 100)  
 MC Flag M2(mouse, Sigma-Aldrich F1804 1:1000)  
 PC mCherry (rabbit, Invitrogen PA5-34974 1: 1000)  
 PC SOS1 (rabbit, Cell Signaling Technology pAb #5890 1: 2000)

### Validation

All antibodies were used for applications validated by antibody suppliers per quality assurance provided by each supplier.

FKBP12 (Abcam ab58072 [1E5-A12]: validated by manufacturer and citations at <https://www.abcam.com/fkbp12-antibody-1e5-a12-ab58072.html>

GFP (Santa Cruz Biotechnology sc-9996) validated by manufacturer and citations at <https://www.scbt.com/p/gfp-antibody-b-2>

β-Actin (Cell Signaling Technology mAb #4970) validated by manufacturer and citations at <https://www.cellsignal.com/products/primary-antibodies/b-actin-13e5-rabbit-mab/4970>

Vinculin (Cell Signaling Technology mAb 4650) validated by manufacturer and citations at <https://www.cellsignal.com/products/primary-antibodies/vinculin-antibody/4650>

PC α-Tubulin (rabbit, Cell Signaling Technology mAb #2144) validated by manufacturer and citations at <https://www.cellsignal.com/products/primary-antibodies/a-tubulin-antibody/2144>

G3BP1 (Santa Cruz Biotechnology sc-365338) validated by manufacturer and citations at <https://www.scbt.com/p/g3bp1-antibody-h-10>

MC Flag M2(mouse, Sigma-Aldrich F1804) validated by manufacturer and citations at <https://www.sigmaaldrich.com/US/en/product/sigma/f3165>

PC mCherry (rabbit, Invitrogen PA5-34974) validated by manufacturer and citations at <https://www.thermofisher.com/antibody/product/mCherry-Antibody-Polyclonal/PA5-34974>

PC SOS1 (rabbit, Cell Signaling Technology pAb #5890) validated by manufacturer and citations at <https://www.cellsignal.com/products/primary-antibodies/sos1-antibody/5890>

## Eukaryotic cell lines

Policy information about [cell lines and Sex and Gender in Research](#)

### Cell line source(s)

HeLa and HEK293T were obtained from the American Tissue Culture Collection (ATCC).

### Authentication

Cell lines were authenticated by the supplier by STR profiling.

### Mycoplasma contamination

Cells were routinely checked for mycoplasma and immediately checked upon suspicion. No cultures tested positive.

### Commonly misidentified lines (See [ICLAC](#) register)

No commonly misused lines were employed.

## Animals and other research organisms

Policy information about [studies involving animals](#); [ARRIVE guidelines](#) recommended for reporting animal research, and [Sex and Gender in Research](#)

Laboratory animals	Primary dorsal root ganglia (DRG) cells were isolated from embryonic (day 17.5-18.5) Sprague-Dawley rats (Charles River Laboratories).
Wild animals	This study did not involve wild animals.
Reporting on sex	This study did not consider sex, and no claims are made based on sex.
Field-collected samples	This study did not include field-collected samples.
Ethics oversight	All animals were housed and experiments were performed in accordance with the US National Institutes of Health (NIH) guidelines for the care and use of laboratory animals, and were approved by Stanford University's Administrative Panel on Laboratory Animal Care. (APLAC # 20608).

Note that full information on the approval of the study protocol must also be provided in the manuscript.

## Flow Cytometry

### Plots

Confirm that:

- The axis labels state the marker and fluorochrome used (e.g. CD4-FITC).
- The axis scales are clearly visible. Include numbers along axes only for bottom left plot of group (a 'group' is an analysis of identical markers).
- All plots are contour plots with outliers or pseudocolor plots.
- A numerical value for number of cells or percentage (with statistics) is provided.

### Methodology

Sample preparation	Adherent cells were lifted with trypsin and transferred into an Eppendorf or conical tube using complete media. Cells were pelleted at 300g and washed three times with PBS. Cells were resuspended in PBS and analyzed on either a BD Accuri C6+ or LSR II flow cytometer.
Instrument	BD Accuri C6+ and BD LSR II, cell sorting was done on a FACSsymphony S6 Sorter.
Software	BD CSampler Plus or FACS Diva were used for data collection, data analysis was performed using the FlowJo software package.
Cell population abundance	After single-cell sorting, populations were verified based on normal distributions positive for the relevant fluorescent proteins.
Gating strategy	Gating was based on FSC and SSC area and doublet removal using FSC-H vs FSC-A.

- Tick this box to confirm that a figure exemplifying the gating strategy is provided in the Supplementary Information.